

Complex Organic Molecules in a Very Young Hot Corino, HOPS 373SW

JEONG-EUN LEE,¹ GISEON BAEK,¹ SEOKHO LEE,² JAE-HONG JEONG,¹ CHUL-HWAN KIM,¹ YURI AIKAWA,³
GREGORY J. HERCZEG,^{4,5} DOUG JOHNSTONE,^{6,7} AND JOHN J. TOBIN⁸

¹*Department of Physics and Astronomy, Seoul National University, 1 Gwanak-ro, Gwanak-gu, Seoul 08826, Korea*

²*Korea Astronomy and Space Science Institute, 776 Daedeok-daero, Yuseong, Daejeon 34055, Korea*

³*Department of Astronomy, University of Tokyo, 7-3-1 Hongo, Bunkyo-ku, Tokyo 113-0033, Japan*

⁴*Kavli Institute for Astronomy and Astrophysics, Peking University, Yiheyuan 5, Haidian Qu, 100871 Beijing, China*

⁵*Department of Astronomy, Peking University, Yiheyuan 5, Haidian Qu, 100871 Beijing, China*

⁶*NRC Herzberg Astronomy and Astrophysics, 5071 West Saanich Rd, Victoria, BC, V9E 2E7, Canada*

⁷*Department of Physics and Astronomy, University of Victoria, Victoria, BC, V8P 5C2, Canada*

⁸*National Radio Astronomy Observatory, 520 Edgemont Rd., Charlottesville, VA 22903*

ABSTRACT

We present the spectra of Complex Organic Molecules (COMs) detected in HOPS 373SW with the Atacama Large Millimeter/submillimeter Array (ALMA). HOPS 373SW, which is a component of a protostellar binary with a separation of 1500 au, has been discovered as a variable protostar by the JCMT Transient monitoring survey with a modest ($\sim 30\%$) brightness increase at submillimeter wavelengths. Our ALMA Target of Opportunity (ToO) observation at ~ 345 GHz for HOPS 373SW revealed extremely young chemical characteristics with strong deuteration of methanol. The dust continuum opacity is very high toward the source center, obscuring line emission from within $0.03''$. The other binary component, HOPS 373NE was detected only in C¹⁷O in our observation, implying a cold and quiescent environment. We compare the COMs abundances relative to CH₃OH in HOPS 373SW with those of V883 Ori, which is an eruptive disk object, as well as other hot corinos, to demonstrate the chemical evolution from envelope to disk. High abundances of singly, doubly, and triply deuterated methanol (CH₂DOH, CHD₂OH, and CD₃OH) and a low CH₃CN abundance in HOPS 373SW compared to other hot corinos suggest a very early evolutionary stage of HOPS 373SW in the hot corino phase. Since the COMs detected in HOPS 373SW would have been sublimated very recently from grain surfaces, HOPS 373SW is a promising place to study the surface chemistry of COMs in the cold prestellar phase, before sublimation.

1. INTRODUCTION

Comets and asteroids reveal that the Solar nebula was rich in water and organic molecules. The recent Rosetta mission also showed that many complex organic molecules (COMs, carbon-bearing molecules made of 6 or more atoms), as well as so-called prebiotic molecules, which could be precursors of amino acids and sugars, exist in the comet 67P/C-G (Altwegg et al. 2017). These organics, together with water, could have been brought to the young Earth's surface by comets and asteroids, which are believed to preserve some compositions from the early stage of star formation. Therefore, the investigation of COMs in the circumstellar environments of

Sun-like young stellar objects is important to infer better the chemical distribution in our Solar system.

Significant progress has been made recently thanks to the ALMA observations of low-mass protostars in various transitions of COMs (Jørgensen et al. 2016; Imai et al. 2016; López-Sepulcre et al. 2017; Sahu et al. 2019; Jacobsen et al. 2019; Yang et al. 2020; Belloche et al. 2020; van Gelder et al. 2020; Yang et al. 2021; Hsu et al. 2022). The hot corinos, where forming stars heat the surrounding material above the sublimation temperature (100 K) of the water ice mantles of dust grains, are very rich in COMs (Ceccarelli et al. 2007), although not all protostars are observed to develop hot corinos. Hot corinos are discovered predominantly toward the youngest and most embedded Class 0 protostars with bolometric luminosities greater than $5 L_{\odot}$, mostly (Belloche et al. 2020; Yang et al. 2020; Hsu et al. 2022). On

the other hand, COMs as rich as those in hot corinos have been rarely detected in disks, except for special cases such as the disk surface of HH 212 (Lee et al. 2019a) and the eruptive disk midplane of V883 Ori (van 't Hoff et al. 2018; Lee et al. 2019b).

Chemical models for COMs require both gas-phase and ice-phase processes in protostellar environments, although ice chemistry is essential to the formation of COMs. During the warm-up phase (20–40 K) developed by protostellar accretion, COMs form efficiently via diffusion of radicals and molecules on grains (Garrod & Herbst 2006). However, in cold prestellar cores, other mechanisms, such as cosmic-ray-induced chemistry (Shingledecker et al. 2018) and non-diffusive reactions (Chang & Herbst 2016; Jin & Garrod 2020), may be important to explain the observed abundances of COMs. We need to explore how organic complexity evolves over the protostellar lifetime to resolve the details of how the formation chemistry of COMs proceeds. Therefore, observations and comparisons of COMs across a wide range of evolutionary stages are critical.

Recently, the ALMA Survey of Orion Planck Galactic Cold Clumps (ALMASOP) project for 11 Class 0 hot corinos clearly showed that the bolometric luminosity positively correlated with the extent and the total number of gas-phase methanol, supporting the thermal sublimation of COMs in the hot corinos (Hsu et al. 2022). In addition, the abundances of specific COMs with respect to CH₃OH in these hot corinos are homogeneous, inferring that chemistry does not evolve much over the short timescale of evolution within Class 0 protostars.

According to Lee et al. (2019b), the COMs in the disk midplane of V883 Ori do show some hints of chemical evolution with higher abundances compared to the hot corino IRAS 16293-2422B (hereafter IRAS 16293B). V883 Ori is in transition from Class I to Class II (Lee et al. 2019b). Therefore, comparisons of relative abundances of COMs over a longer evolutionary timescale, covering the very beginning stage of Class 0 through Class II, are feasible to explore the chemical evolution of COMs. Unfortunately, detecting COMs in both extremely young Class 0 objects with very low luminosities as well as Class II objects is challenging because their luminosities are not high enough to develop a detectable region of COMs emission. One desirable solution is to utilize accretion bursts, which can extend the COMs sublimation region to larger radii, as demonstrated in V883 Ori.

Episodic accretion (Hartmann & Kenyon 1996) is now accepted as the standard accretion model in the low mass star formation, and thus, the burst accretion is a

common phenomenon throughout the protostellar evolution with more frequent and more powerful accretion bursts in earlier evolutionary stages. Recently, surveys at long wavelengths (e.g. Scholz et al. 2013; Rebull et al. 2014; Antonucci et al. 2014; Lucas et al. 2017; Johnstone et al. 2018; Fischer et al. 2019; Lee et al. 2021; Park et al. 2021; Zakri et al. 2022) have evaluated the statistics of accretion variability during the earlier stages of protostellar evolution. Therefore, we are now in a better situation to study COMs even in the earliest protostars.

HOPS 373, a young protostellar binary system with a separation of 1500 AU (Tobin et al. 2015, 2020), was discovered as a variable with $\sim 30\%$ brightness increase at 850 μm by the JCMT Transient monitoring survey (Yoon et al. 2022). HOPS 373 has been classified as a PACS Bright Red Source (Stutz et al. 2013), which is consistent with an early stage of a Class 0 protostar. Following this JCMT Transient discovery, we triggered our ALMA Target of Opportunity (ToO) program to study the sublimated COMs by the recent (2021 March) burst event (Yoon et al. 2022) in HOPS 373 with almost the same spectral setup used for V883 Ori (Lee et al. 2019b). The identical observations of two eruptive sources in very distinct evolutionary stages within the same star-forming environment of the Orion cloud provide us an important opportunity to study the chemical evolution of COMs from the protostellar envelope to the disk.

2. OBSERVATIONS

HOPS 373 was observed with ALMA during Cycle 7 (2019.1.00386T, PI: Jeong-Eun Lee) on 2021 August 2 and 6. The coordinates of the phase center are $\alpha = 05^{\text{h}}46^{\text{m}}30^{\text{s}}.905$ and $\delta = -00^{\text{d}}02^{\text{m}}35^{\text{s}}.200$ (J2000). Two observations were carried out with slightly different configurations: the earlier observation has the baseline range from 46.8 m to 5.6 km with thirty-eight 12-m antennas, while the later observation consists of the baselines from 70 m to 6.9 km with thirty-nine antennas. The total observing time on HOPS 373 was 30.5 minutes for each observation. The eight spectral windows were set for 335.327–335.445 GHz, 336.485–336.719 GHz, 336.993–337.110 GHz, 338.306–338.775 GHz, 346.937–347.406 GHz, 349.162–349.396 GHz, 350.035–350.152 GHz, 350.353–350.470 GHz, each with a spectral resolution of 244.141 kHz ($\sim 0.2 \text{ km s}^{-1}$). This setup contains HDO $3_{3,1} - 4_{2,2}$, C¹⁷O $3 - 2$, CH₃OH $7_{\text{k}} - 6_{\text{k}}$, H¹³CO⁺ $4 - 3$, CCH $\text{N} = 4 - 3$, $\text{J} = 7/2 - 5/2$, $\text{F} = 4 - 3$ and $\text{F} = 3 - 2$ lines, and many COMs including isotopologues.

The data were initially calibrated using the CASA 6.1.1.15 pipeline (McMullin et al. 2007). The quasar J0510+1800 was used as a bandpass and amplitude cal-

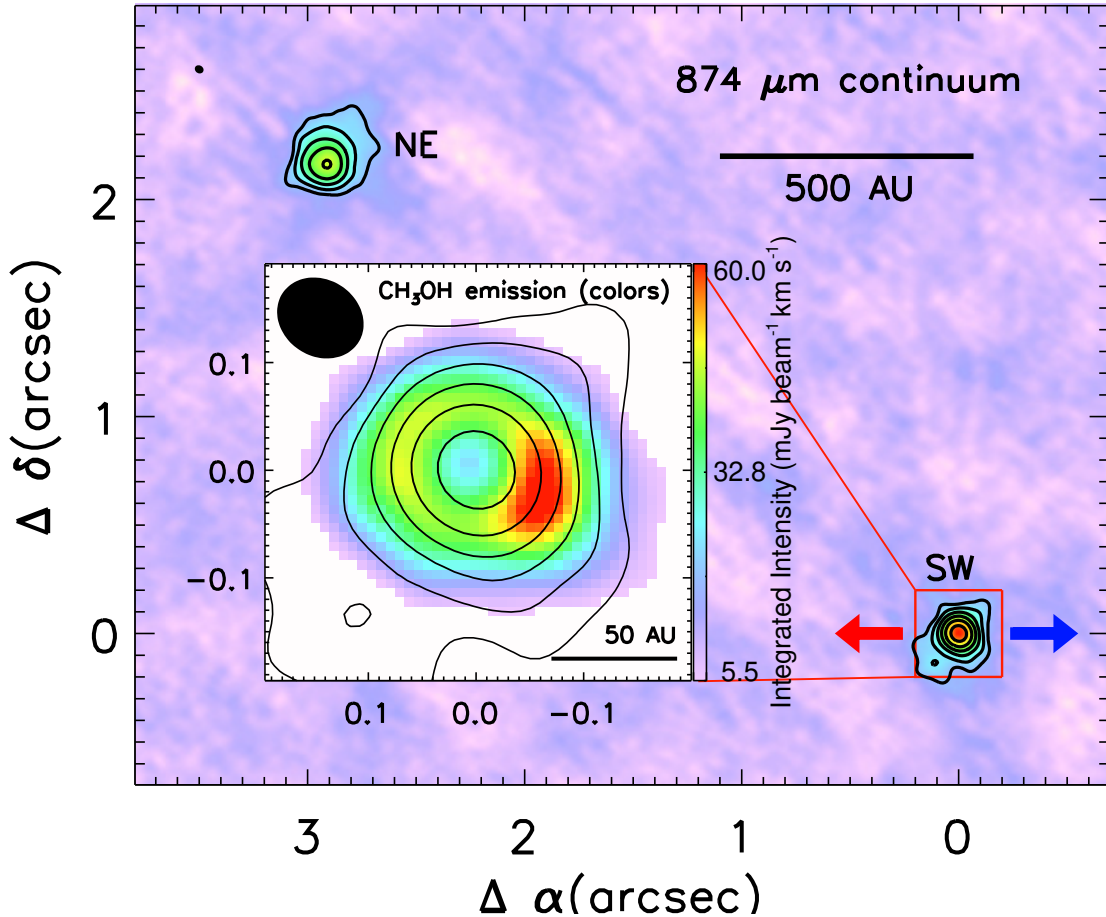


Figure 1. The ALMA Band 7 continuum image. The contours are 10, 20, 40, 80, 160, and 320 σ ($1 \sigma = 0.11 \text{ mJy beam}^{-1}$). The red and blue arrows denote the outflow directions of red- and blue-shifted components, respectively, in a small scale in the vicinity of HOPS 373SW. The inset presents the integrated intensity map of the averaged CH_3OH (color image) with the same contours for the continuum intensity. The CH_3OH intensity is integrated within $\pm 1 \text{ km s}^{-1}$ after correcting for the envelope velocity profile using the $^{13}\text{CH}_3\text{OH}$ intensity weighted velocity map (the second top left panel of Figure 2), and only the integrated intensity over the 5σ ($1 \sigma = 1.1 \text{ mJy beam}^{-1} \text{ km s}^{-1}$) is presented in the color image. The observed beam is presented in the filled black ellipse on the top left corner.

ibrator, and the nearby quasar J0532+0732 was used as a phase calibrator. Only a phase self-calibration with a solution interval of ‘inf’ was applied for better imaging. Only the baselines with the UV distance longer than 100 m were used **to remove** stripe features shown in the continuum image.

The natural weighting was used to obtain a high signal-to-noise (S/N) ratio as well as a high spatial resolution; the beam has a size of $0.08'' \times 0.07''$ ($34 \text{ au} \times 30 \text{ au}$) with a position angle of $\sim 55^\circ$. A dust continuum image was produced using line-free channels. The RMS noise levels of the line cube and the continuum image are ~ 3 and $0.11 \text{ mJy beam}^{-1}$, respectively.

3. EMISSION DISTRIBUTION

3.1. Continuum emission

Both continuum sources in the binary system (Yoon et al. 2022) are well resolved, as presented in Figure 1. In this observation, the flux densities of the NE and SW sources are $75.1 (\pm 1.4)$ and $90.4 (\pm 1.4) \text{ mJy}$ at 0.87 mm , respectively. However, their previous flux densities were $85.0 (\pm 3.3)$ and $81.8 (\pm 1.7) \text{ mJy}$ at 0.89 mm , respectively, in Yoon et al. (2022), where the two observations in 2016 and 2017 were averaged to increase the S/N ratio since the fluxes did not change much between the two observations. Each flux density in two different observations cannot be directly compared because of two different observational parameters and the absolute calibration error (see, e.g., Francis et al. 2020). However, the flux ratio between two sources (SW/NE) within the same observation must be robust, and the

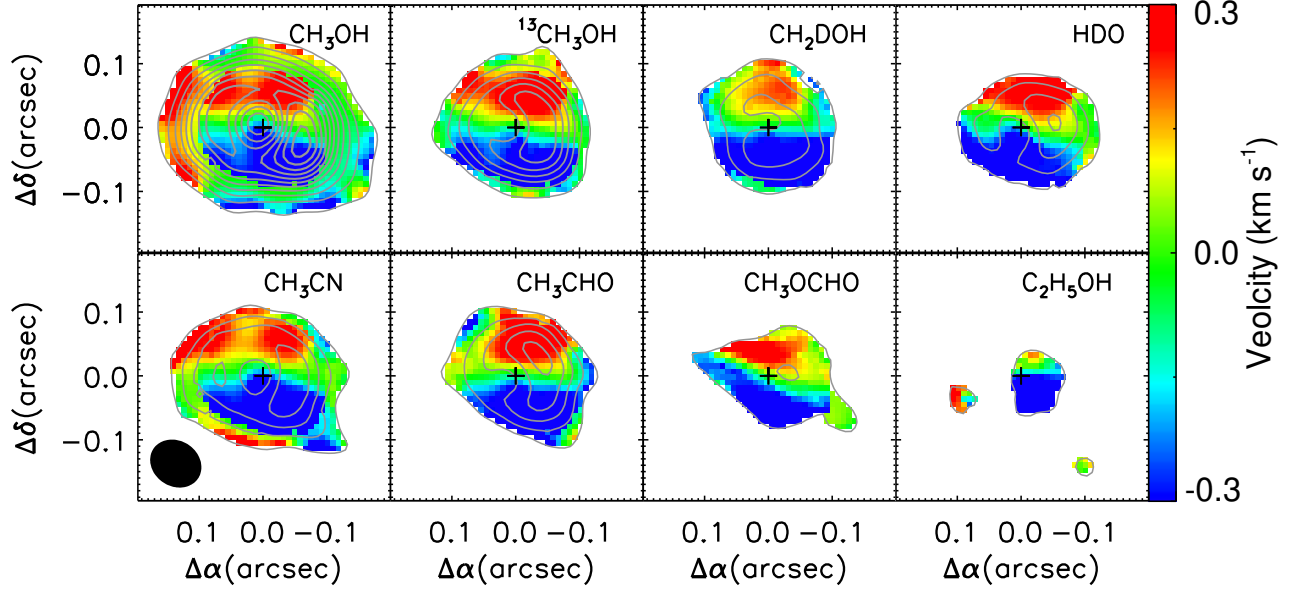


Figure 2. Intensity weighted velocity maps (colors) and integrated intensity maps (contours) of 8 different molecular lines. Two isolated lines are averaged each for CH_3OH , $^{13}\text{CH}_3\text{OH}$, and CH_3CHO . The start and step of contours are 5σ . The rms noise levels are 1.1, 1.2, 2.1, 2.0, 2.3, 1.6, 1.9, and 2.3 $\text{mJy beam}^{-1} \text{ km s}^{-1}$ for CH_3OH , $^{13}\text{CH}_3\text{OH}$, CH_2DOH , HDO , CH_3CN , CH_3CHO , CH_3OCHO , and $\text{C}_2\text{H}_5\text{OH}$, respectively. The cross denotes the position of the continuum peak. The observed beam is presented in the lower left panel. The source velocity of 10.13 km s^{-1} is adopted

ratio has increased from 0.96 to 1.20 by a factor of 1.25 (± 0.1) supporting the SW source as the primary brightening source.

The mass of each target may be estimated from the continuum flux by

$$M = \frac{F_V d^2}{\kappa_V B_V(T_{\text{dust}})}, \quad (1)$$

where F_V is the observed flux, d is the distance to HOPS 373, κ_V is the dust opacity, and $B_V(T_{\text{dust}})$ is the Planck function with the dust temperature of T_{dust} . We adopt an average dust temperature of 65 K by using the method of Tobin et al. (2020) and the bolometric luminosity of $5.3 L_\odot$ (Kang et al. 2015), the OH5 dust opacity $\kappa_V = 1.84 \text{ cm}^2 \text{ g}^{-1}$ (Ossenkopf & Henning 1994), and a gas-to-dust ratio of 100. The estimated mass could be highly uncertain due to the continuum optical depth and the dust opacity (Williams & Cieza 2011). The properties of two continuum sources are summarized in Table 1.

3.2. Molecular emission

Except for C^{17}O , all line emission is detected only in HOPS 373SW. The line emission is also affected significantly by the dust continuum opacity (Harsono et al. 2018; Lee et al. 2019b); as seen in the inset of Figure 1, the molecular emission of HOPS 373SW shows a hole inside the radius of $\sim 0.03''$. Figure 2 shows 8 molecular line intensity distributions (contours) on top

of the intensity-weighted velocity maps (colors) in HOPS 373SW. All molecular emission decreases toward the center (due to the dust continuum opacity) with molecular emission peaks located $\sim 0.06''$ away from the center to the west. The blue-shifted outflow cavity is located to the west. Therefore, the western part of the emission faces less extinction. On the other hand, the emission in the east part is extinct by the thick envelope material beyond the red-shifted cavity wall. The C^{17}O J=3–2 line is not present in Figure 2 because it shows the inverse P-Cygni profile with the red-shifted absorption against the continuum, indicative of infall (Evans et al. 2015).

The intensity-weighted velocity maps of all molecular lines (Figure 2) clearly show the velocity gradient from the north to the south, indicative of a rotational motion perpendicular to the known CO outflow direction (Yoon et al. 2022). On the other hand, the CH_3OH map (the upper left of Figure 2) shows another velocity gradient consistent with the EW outflow direction beyond $0.1''$ (S. Lee et al. submitted.). Therefore, we extract the spectra from the emission area between $0.03''$ and $0.1''$ in the western semicircle to increase the S/N and minimize the outflow effect. Inside $0.03''$, the dust continuum opacity is high enough to produce sub-continuum absorption in molecular lines.

Even within $0.1''$, the eastern hemisphere is largely affected by the outflow, particularly in the CH_3OH lines. Figure 3(a) presents the line width distribution of the

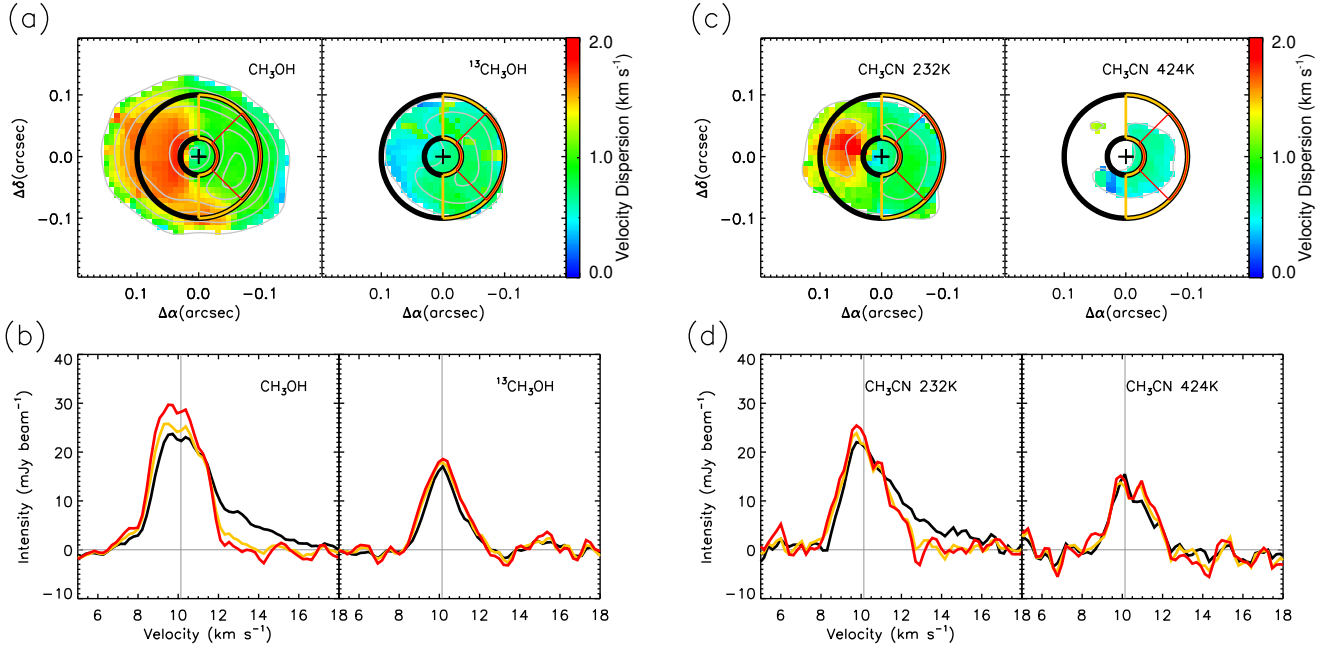


Figure 3. Velocity dispersion (an image) and the averaged spectra for the CH_3OH and $^{13}\text{CH}_3\text{OH}$ lines. (a) The contours indicate the integrated intensity and the start and step of contours are 10σ . (b) The spectra are averaged within the regions outlined with the same colors (black, orange, and red) in the top panels. The vertical lines indicate the source velocity (10.13 km s^{-1}) measured from the $^{13}\text{CH}_3\text{OH}$ spectra shown in the bottom right panel. (c) and (d) panels are the same as (a) and (b) except for the CH_3CN lines with two different upper energy levels.

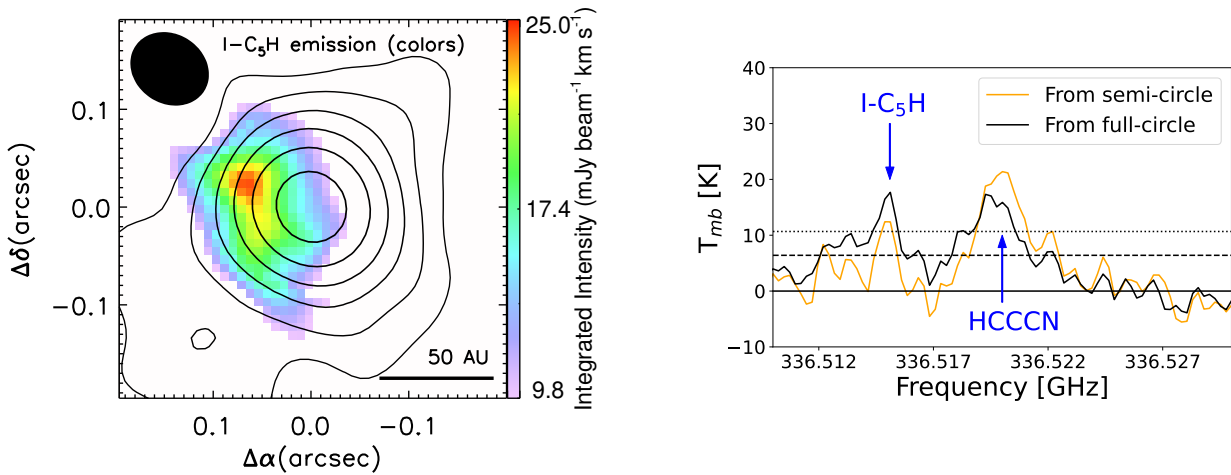


Figure 4. The integrated intensity map (color) of the C_5H line at 336.5148 GHz (left) and the spectra extracted from the full circle and the western semicircle as marked in black and orange colors, respectively, in Figure 3 (right). The emission distributes only in the eastern part of HOPS 373SW, where lines are affected by outflows/jets. Therefore, the C_5H line disappears in the spectrum extracted from the western semicircle (right). In the left panel, contours show the distribution of the dust continuum emission, and the levels are the same as those in Figure 1. The integrated intensity over 5σ ($1 \sigma = 1.96 \text{ mJy beam}^{-1} \text{ km s}^{-1}$) is presented in the color image. The dashed and dotted lines in the right panel represent the $3 \sigma_{T_{\text{mb}}}$ and $5 \sigma_{T_{\text{mb}}}$ ($1 \sigma_{T_{\text{mb}}} = 2.2 \text{ K}$) levels, respectively.

CH_3OH and $^{13}\text{CH}_3\text{OH}$ lines, and the bottom panel (b) compares the line profiles extracted from the regions with the same color boundaries. Unlike the CH_3OH lines extracted from the sectors for the orange and red color boundaries tracing semicircles in the west, the CH_3OH

line extracted from the full annulus traced by the black color boundary shows a red-shifted high-velocity wing structure. This effect of outflow appears differently in different transitions of a given molecule. A lower energy transition of CH_3CN ($E_u=232 \text{ K}$) has a high-velocity dis-

persion in the eastern hemisphere as seen in the CH₃OH emission, while its higher energy transition of $E_u=424$ K is not affected by the outflow (Panels (c) and (d) in Figure 3).

Other complex molecular emission is also affected by the outflows. The line at 336.5148 GHz that is clearly detected in the spectrum extracted over the full annulus disappears in the spectrum extracted from the western semicircle, as seen in the right panel of Figure 4. This line is possibly a C₅H line. The integrated intensity map of the line is presented in the left panel of Figure 4; the emission distributes only in the eastern part of HOPS 373SW, where the red-shifted outflow component contributes to the molecular excitation (Figure 3).

The line profiles extracted from the sector with the red boundary, where all molecular emission is the strongest, are consistent with those extracted from the orange boundary sector, with similar line intensities. Therefore, we extract the spectra from the western semicircle inside the orange boundary to avoid the effect of the outflow and to maximize the S/N of each spectrum. The extracted spectra from the western region outlined with the orange semicircle are used for the comparison with V883 Ori (Figure 5), the rotation diagram analysis (Figure 6), and the detailed line fitting (Figure 7).

4. LINE SPECTRA

4.1. Comparison with V883 Ori

The extracted spectra are presented in Figure 5 in the gray line. These spectra were corrected for the velocity shifts caused by the rotational motion. We derived the rotation velocity structure using the ¹³CH₃OH lines, which is presented in the upper second panel of Figure 2 as the color image. The rotation motion in HOPS 373SW probably originates from the envelope rather than the disk (Section 5.1). In fact, the infalling envelope is well traced by the inverse P-Cygni profile of C¹⁷O J=2–1, which shows the red-shifted (i.e., at the lower frequency) absorption below the continuum (see the line profile marked with the magenta circle around 337.06 GHz in Figure 5.)

The spectra of V883 Ori (Lee et al. 2019b) are also plotted in Figure 5 with the red dotted line for comparison. The spectra of V883 Ori were extracted over the annulus between 0.1'' and 0.2'' in radius and also corrected for the disk rotation (Lee et al. 2019b). The ¹³CH₃OH line peak intensities of V883 Ori are about four times weaker than those of HOPS 373SW, so in Figure 5, the spectra of V883 Ori are scaled up by a factor of 4 for the comparison with the HOPS 373SW spectra. This lower intensity of V883 Ori compared to HOPS 373 is probably caused by a combination of higher dust continuum

optical depth and lower gas temperature *at the emission peak beyond the emission hole* in the disk of V883 Ori ($\sim 0.15''$) than in the envelope of HOPS 373 ($\sim 0.06''$).

V883 Ori is an eruptive young star with a bolometric luminosity of $\sim 200 L_{\odot}$ (Furlan et al. 2016), in transition from Class I to Class II, whereas HOPS 373SW is a very young Class 0 object with the bolometric luminosity of $5.3 L_{\odot}$. Therefore, one could expect that the chemical characteristics inherited from the natal molecular cloud have not been modified much in HOPS 373SW, while the chemistry in V883 Ori may have evolved significantly in the dense protoplanetary disk.

From a simple comparison of the line intensities, appreciable differences between HOPS 373SW and V883 Ori are found, as follows:

- (1): The HDO line is clearly detected in HOPS 373SW without any confusion by neighboring lines, while it is marginally detected in V883 Ori.
- (2): The C¹⁷O line shows red-shifted absorption against the continuum in HOPS 373, indicative of infall in the inner envelope.
- (3): The CH₃OH $v_t=2$ lines have **only** been detected in HOPS 373, suggesting a higher gas temperature than in V883 Ori.
- (4): Many strong CH₂DOH, CHD₂OH, and CD₃OH lines are detected in HOPS 373SW. The lines are as strong as the main isotopic methanol lines, indicative of a very high D/H ratio in methanol even in consideration of the optically thick CH₃OH lines.
- (5): The CH₃CHO line intensity relative to that of CH₃OH is weaker in HOPS 373SW than in V883 Ori, whereas one line of CH₂DCHO is detected at 335.406 GHz with a similar strength to the CH₃CHO $v_t=1$ line at 335.382 GHz in HOPS 373SW.
- (6): The CH₃OCHO line intensity relative to that of CH₃OH is mostly weaker in HOPS 373SW than V883 Ori.
- (7): The C₂H₅OH lines are detected clearly in HOPS 373SW, unlike in V883 Ori.
- (8): The c-H₂COCH₂ and t-HCOOH lines, which are detected in V883 Ori, are not detected in HOPS 373SW.

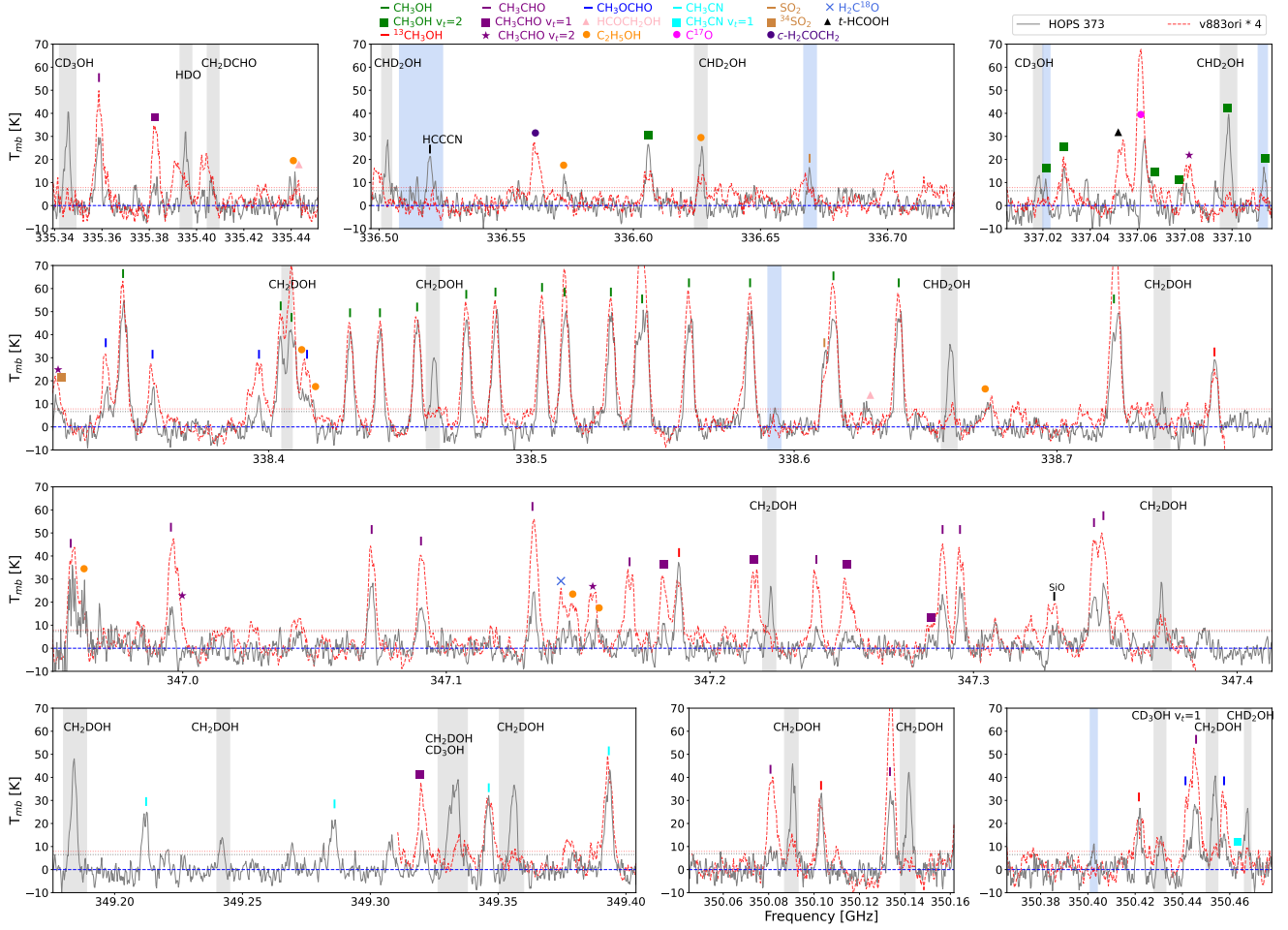


Figure 5. The ALMA band 7 spectra of HOPS 373SW (gray solid line) compared with those of V883 Ori (red dotted line, Lee et al. 2019b). The spectral setup is almost the same in the two observations. The spectra of V883 Ori are extracted over the full annulus between $0.1''$ to $0.2''$ in radius, while the spectra of HOPS 373SW are extracted over the western semicircle between $0.03''$ to $0.1''$ (see Figure 3). The V883 Ori spectra have been scaled up by a factor of 4 to better compare with those of HOPS 373SW. The identified lines are marked with bars and symbols with different colors right above individual lines. The newly detected lines in HOPS 373SW and the lines much stronger than those of V883 Ori are shaded; the gray shades denote deuterated species, while the purple shades indicate unidentified or tentatively identified lines. The RMS noises ($\sigma_{T_{\text{mb}}}$) are, before scaling up, 0.65 and 0.66 K for the spectral windows around 330 GHz and 340 GHz, respectively, in V883 Ori. In HOPS 373SW, the RMS noises ($\sigma_{T_{\text{mb}}}$) are 2.2 and 2.3 K for the spectral windows around 330 GHz and 340 GHz, respectively. The red and gray dotted horizontal lines represent the $3\sigma_{T_{\text{mb}}}$ level.

4.2. The LTE analysis of COMs lines

The excitation diagrams of eight species are presented in Figure 6. Compared to those of V883 Ori (Lee et al. 2019b, ~ 100 K), the excitation temperatures are very high; the excitation temperatures of CH_2DOH and CH_3CHO are ~ 160 K, and those of CHD_2OH and CH_3CN are even higher ~ 300 K. HH 212 also shows high excitation temperatures of $150\sim 160$ K (Lee et al. 2019a). On the other hand, in most of ALMASOP hot corinos, the excitation temperatures of CH_2DOH are lower than 100 K (Hsu et al. 2022).

For more detailed analyses, we adopt XCLASS, which can identify the detected lines and derive the column densities and the excitation temperatures of species by inspecting all transitions of a species within the observed frequency range. We first fitted the line transitions of individual species independently to identify detected transitions and derive rough estimations of fitting parameters such as column density, excitation temperature, and line width for a specific molecule. Then, we fitted simultaneously ten molecules ($\text{CH}_3\text{OH } v_1=2$, CD_3OH , $^{13}\text{CH}_3\text{OH}$, CH_2DOH , CHD_2OH , CH_3CHO , CH_3OCHO , $\text{C}_2\text{H}_5\text{OH}$, CH_3CN , HCOCH_2OH), whose lines are heavily blended, especially in the 4th and 8th spectral win-

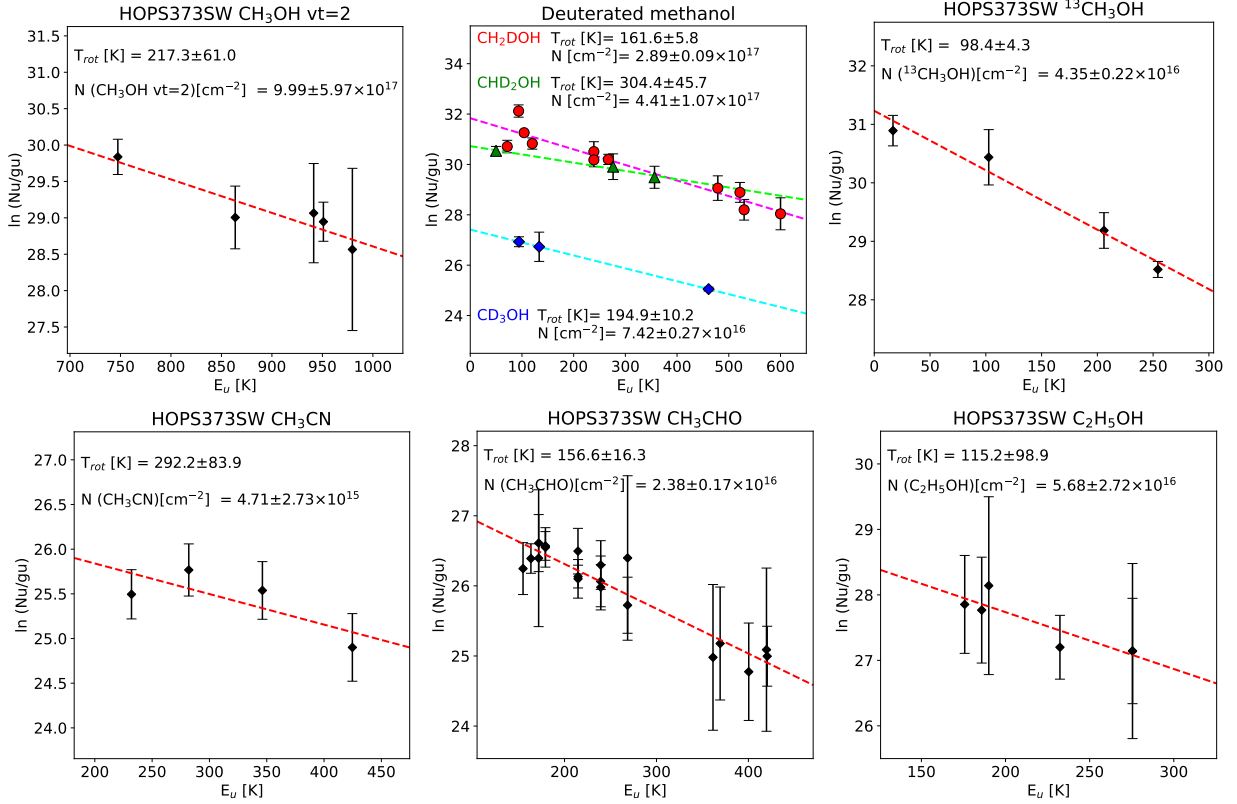


Figure 6. The excitation diagrams of CH_3OH ($v_t=2$), CH_2DOH , CHD_2OH , CD_3OH , $^{13}\text{CH}_3\text{OH}$, CH_3CN , CH_3CHO , and $\text{C}_2\text{H}_5\text{OH}$. The isolated lines that can be fitted with a Gaussian profile are used for these excitation diagrams.

downs, to provide the final column densities and excitation temperatures listed in Table 4. The other molecules are fitted individually. Figure 7 shows the spectra fitted by XCLASS on top of the observed spectra. Before the XCLASS fittings, lines are corrected for the velocity shifts caused by rotation, and the central velocity is shifted to zero.

XCLASS considers the dust continuum optical depth in the line fitting process using a given value of the molecular hydrogen column density. An optical depth (τ_c) for the dust continuum emission reduces the molecular line intensity by $\exp(-\tau_c)$ (Yen et al. 2016; Lee et al. 2019b, 2020). We derive the average τ_c over the western semicircle marked by the orange color boundary in Figure 3, where the line spectra were extracted, using a simple model. We assumed that the dust temperature distribution follows $T_{0.03''} \times \sqrt{0.03''/r}$, where $T_{0.03''}$ is the dust temperature at $r=0.03''$, and dust emission is very optically thick near the continuum peak; then, the observed continuum peak could be reproduced with $T_{0.03''} \sim 105$ K. Median values of the dust continuum intensity ($J(T)$) and the model dust temperature over $0.03''$ to $0.1''$ in the western semicircle (outlined with the orange boundary) are 34 K and ~ 70 K, respectively, which result in τ_c of 0.66. Finally, a molecular hydrogen

column density of $\sim 8.9 \times 10^{24} \text{ cm}^{-2}$ is derived from τ_c by assuming the OH5 dust opacity $\kappa_V = 1.84 \text{ cm}^2 \text{ g}^{-1}$ (Ossenkopf & Henning 1994), the gas-to-dust ratio of 100, and the mean molecular weight of 2.4.

The column densities derived from the XCLASS fitting are generally higher than the values derived from the rotation diagrams, except for CH_3CN . However, considering the uncertainties, they are consistent within a factor of 2, at maximum. Typically, the derived temperatures are also consistent at the level of a few 10s of degrees although those of CHD_2OH , CD_3OH , and CH_3CN show rather large differences of 70 to 90 K. We believe that the values from the XCLASS fitting are more reliable because the dust opacity, as well as self-absorption, has been taken into account by XCLASS.

5. DISCUSSION

5.1. The origin of COMs emission: hot corino vs. disk

The clear velocity structure of rotation is shown in the intensity weighted velocity maps of most detected simple or complex molecules (see examples in Figure 2). In the early evolutionary stage, particularly in the extremely young Class 0 object, the kinematics may be dominated by the envelope rather than the disk even at this sub-arcsecond resolution since the disk may not be



Figure 7. The spectra of HOPS 373SW fitted with XCLASS. Different colors represent the line transitions of different species. Black solid/dashed lines represent the tentatively identified lines. C_2H_5OH lines are largely blended with other species. Thus, to clearly distinguish, we shaded C_2H_5OH lines with an orange color. The identified lines are listed in Table 2 and Table 3, and the column density and excitation temperature best fitted for each species are summarized in Table 4 along with its abundance relative to CH_3OH . The dashed and dotted horizontal lines represent the $1\sigma_{T_{mb}}$ and $3\sigma_{T_{mb}}$ levels, respectively.

well developed yet. The position-velocity diagram of a $^{13}CH_3OH$ line (Figure 8) does not show a Keplerian disk rotation feature, although a detailed examination of the kinematics, beyond the scope of this paper, is required to confirm the real origin of COMs emission. Nevertheless, as we will see from the emission radius, we speculate that the detected rotational motion in HOPS 373SW is likely of the dense inner envelope, and the disk radius could be much smaller than the radius of continuum emission (~ 65 au).

In general, the hot corino sources with rich COMs emission, such as IRAS 16293B (Jørgensen et al. 2016), B335 (Imai et al. 2016), and L483 (Jacobsen et al. 2019), do not have well-developed large disks. In contrast, protostars with well-developed massive disks with sizes

~ 100 au (Sakai et al. 2014; Artur de la Villarmois et al. 2019; Lee et al. 2020; van’t Hoff et al. 2020) lack rich COMs emission, suggesting that COMs are frozen on grain surfaces in the dense disk midplane since the current luminosity of those protostars is not high enough to extend the water snow line to a large radius in the disk midplane. In this sense, the rich COMs emission detected in HOPS 373SW very likely originates from the hot corino, the hot inner envelope.

The water sublimation radius can be another discriminator for the origin of COMs emission. The water sublimation radius in a hot corino can be estimated from the source bolometric luminosity (Bisschop et al. 2007; van’t Hoff et al. 2022). According to the 1-D radiative transfer models of massive protostars by Bisschop et al.

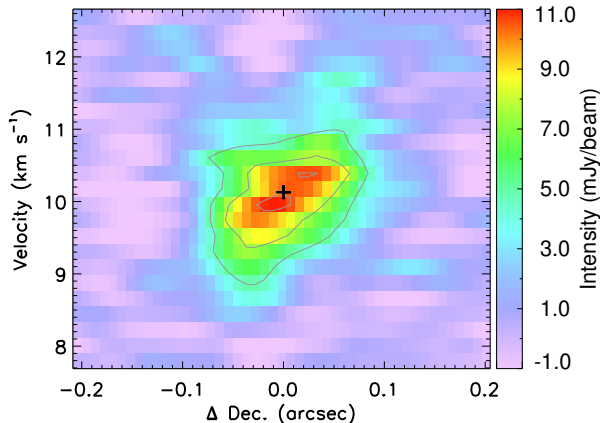


Figure 8. Position velocity diagram of $^{13}\text{CH}_3\text{OH}$ along the Declination. The cross indicates the source velocity (10.13 km s^{-1}) and the continuum peak position. The contours are 5, 8, 11 σ ($1 \sigma = 1.8 \text{ mJy beam}^{-1}$).

(2007), the water sublimation radius follows the equation, $R_{\text{snow}} \sim R(100 \text{ K}) = 15.4 \sqrt{L/L_{\odot}}$ au. This relation can also be applied to low-mass protostars (van’t Hoff et al. 2022). With the luminosity of $5.3 L_{\odot}$, from the above equation, the water sublimation radius of HOPS 373SW is anticipated as ~ 35 au, which is consistent with the boundary ($\sim 0.1''$) of COMs emission. This consistency also supports that the COMs emission originates from the hot corino rather than a disk in HOPS 373SW.

The eruptive disk source, V883 Ori, has a bolometric luminosity of $\sim 200 L_{\odot}$, which should develop the water sublimation radius around 220 au in a hot corino. However, the estimated snow line in V883 Ori is located between 40 au and 100 au (Lee et al. 2019b; Leemker et al. 2021; Tobin et al. 2023). This indicates that the relation between water sublimation radius and luminosity is different in hot corinos and disks, probably due to their different densities and dust properties (Chiang & Goldreich 1997).

5.2. Deuteration of CH_3OH and CH_3CHO

The most remarkable chemical characteristics in HOPS 373SW are very high D/H ratios of methanol and the strong HDO and CH_2DCHO lines. The detection of even doubly and triply deuterated methanols has been confirmed in HOPS 373SW, thanks to the newly calculated spectroscopic data (Coudert et al. 2021; Ilyushin et al. 2022). Table 5 lists the column density ratios of deuterated species as well as the D/H ratios corrected for the statistical effect (Parise et al. 2004).

In Table 5, the column density ratio between CH_2DOH and CH_3OH is 0.36. The ratio can be 0.13 if we use the $^{13}\text{CH}_3\text{OH}$ column density and the carbon iso-

topic ratio ($^{12}\text{C}/^{13}\text{C}$) of 60 (Lee et al. 2019b). However, many CH_3OH $v_t=2$ lines, which are optically thin, have been detected in HOPS 373SW. Therefore, for the calculation of the D/H ratio, we adopt the column density derived from the $v_t=2$ transitions, which is, in fact, not very different from what has been derived from the $v_t=0$ lines with XCLASS. In addition, the excitation temperature derived from the $v_t=2$ lines is similar to those of deuterated methanol. The $^{12}\text{C}/^{13}\text{C}$ ratio is about 20 if we use the CH_3OH column density derived from the CH_3OH $v_t=2$ lines and the $^{13}\text{CH}_3\text{OH}$ column density. This low value is consistent with the value derived in IRAS 16293B (Jørgensen et al. 2018).

HOPS 373SW is the second hot corino where the detection of CD_3OH has been confirmed, following IRAS 16293B (Ilyushin et al. 2022). For HOPS 373SW, the column density ratio between CHD_2OH and CH_2DOH is 0.75, which is much higher than the ratio between CH_2DOH and CH_3OH . This trend is consistent with other hot corinos (Drozdovskaya et al. 2022) and prestellar cores (Lin et al. 2023). Figure 9 shows that the column density ratios of singly and doubly deuterated methanols in HOPS 373SW are higher than other hot corinos and similar to the highest values seen in prestellar cores.

A transition of CH_3OD , another singly deuterated methanol, is covered in our spectral setup. An emission line is clearly detected with $> 3\sigma$ (T_{mb} of $\sim 10 \text{ K}$) at 347.308432 GHz (Anderson et al. 1988; Duan et al. 2003). This tentative detection of CH_3OD also supports the high deuteration of HOPS373 SW since the deuteration in the OH functional group is less efficient compared with the CH_3 functional group (Nomura et al. 2022).

As seen in Table 5, the D/H ratios with the statistical corrections are higher for multi-deuterated methanols than the mono-deuterated methanol by a factor of ~ 3 , suggesting that subsequent hydrogen abstractions may be more probable after the first deuteration of methanol (Drozdovskaya et al. 2022). According to the chemical models of deuterated ices by Taquet et al. (2014), the D/H ratio of deuterated methanol can be enhanced if a hot corino had a higher density in the prestellar stage. In addition, the D/H ratios of singly deuterated methanol and singly deuterated acetaldehyde are similar to $\sim 10 \%$, which is the highest level for hot corinos (Drozdovskaya et al. 2022). This enhanced deuteration, which is believed to occur in the cold prestellar phase (Lee & Bergin 2015), strongly suggests that HOPS 373SW is a very young hot corino that retains the memory of the cold phase since the D/H ratio decreases with protostellar evolution (Aikawa et al. 2012). In addition, the similar D/H ratio of methanol and ac-

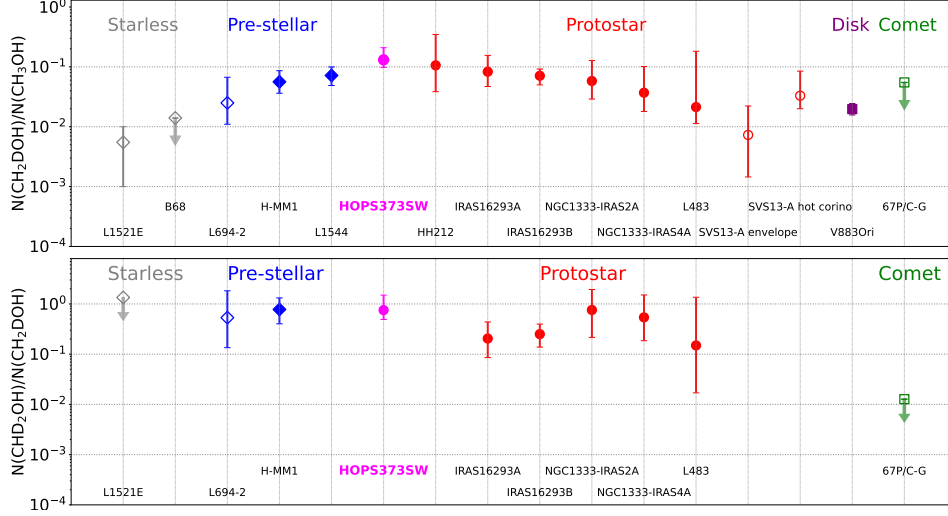


Figure 9. Column density ratios of $\text{CH}_2\text{DOH}/\text{CH}_3\text{OH}$ (upper panel) and $\text{CHD}_2\text{OH}/\text{CH}_2\text{DOH}$ (lower panel). Filled and open symbols indicate single-dish and interferometric observations, respectively. Except for HOPS 373SW, data have been obtained from the literature; L1521E, B68, L694-2, and H-MM1 from Lin et al. (2023), L1544 from Chacón-Tanarro et al. (2019), HH212 from Lee et al. (2019a), IRAS16293A and IRAS16293B from Jørgensen et al. (2018), Manigand et al. (2019), and Drozdovskaya et al. (2022), NGC1333-IRAS2A and NGC1333-IRAS4A from Taquet et al. (2019), L483 from Agundez et al. (2019), SVS13 from Bianchi et al. (2017), V883Ori from Lee et al. (2019b), and 67P/C-G from Drozdovskaya et al. (2021)

etaldehyde indicate that the two molecules formed over a similar timescale and/or within a similar layer of the ices (Taquet et al. 2014).

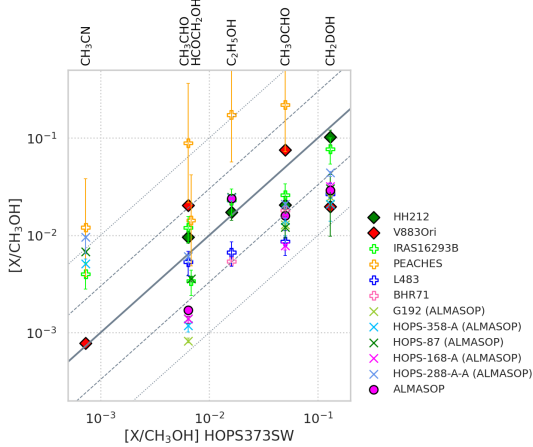


Figure 10. Comparison of COMs abundances with other hot corinos and disks. The abundances toward HOPS 373SW and other sources (Table 6) are on the x- and y-axis, respectively. Some abundances from the literature are rescaled to be consistent with our assumption of $^{12}\text{C}/^{13}\text{C}=60$. The diagonal lines denote equal abundances (solid) and abundances factors of 3 (dashed) and 10 (dotted) above or below those in HOPS 373SW.

5.3. COMs abundances vs. evolution

The region of COMs emission in HOPS 373SW is about 40 au, which is consistent with the water sublimation radius developed in the envelope by its lumi-

nosity (Bisschop et al. 2007; van’t Hoff et al. 2022) as discussed in Section 5.1. Table 6 and Figure 10 compare the abundances of COMs detected in HOPS 373SW with those of other hot corinos in Orion (ALMASOP; Hsu et al. 2022), HH 212 (Lee et al. 2019a), and V883 Ori (Lee et al. 2019b) as well as other well studied hot corinos, including IRAS 16293B (Jørgensen et al. 2016) and the Perseus ALMA Chemistry Survey (PEACHES) samples (Yang et al. 2021). We use the $^{13}\text{CH}_3\text{OH}$ lines to derive the COMs abundances respective to CH_3OH for consistency with other studies. In general, $^{13}\text{CH}_3\text{OH}$ or $\text{CH}_3^{18}\text{OH}$ has been adopted to calculate the column density of CH_3OH because the CH_3OH lines are optically thick. According to our XCLASS fitting results, the optical depths are as high as ~ 40 for some transitions of CH_3OH , while the optical depths of all $^{13}\text{CH}_3\text{OH}$ transitions are below 1.

The abundances of the ALMASOP hot corinos and HH 212, which were obtained from the literature, were scaled down by a factor of 1.2 in Table 6 because they were originally calculated by adopting the $^{12}\text{C}/^{13}\text{C}$ ratio of 50 (Kahane et al. 2018), while we use the ratio of 60 (Langer & Penzias 1993) for HOPS 373SW and V883 Ori. Note, however, that the true $^{12}\text{C}/^{13}\text{C}$ may be about 20 for HOPS 373SW (see Section 5.1) and potentially V883 Ori (Jeong et al. in prep.), much lower than 60. In addition to the mean abundances taken over 11 ALMASOP sources, we also list the COMs abundances of 5 individual hot corinos, which have the richest COMs

spectra among the ALMASOP sample, separately at the bottom of Table 6.

In general, the PEACHES sample (orange cross in Figure 10) has significantly higher COMs abundances than HOPS 373SW. The most diverse abundance distribution is found for CH_3CN and CH_3CHO . In all other hot corinos, compared to HOPS 373SW, CH_3CN is much more abundant, while other COMs such as HCOCH_2OH and CH_3OCHO are less abundant. The ratio between CH_3CN and CH_3OH has been suggested as an evolutionary indicator (Öberg et al. 2014), since the formation of CH_3CN on grain surfaces is sensitive to the physical conditions and evolutionary timescales in individual sources (Bonfand et al. 2019). Therefore, the low ratio of CH_3CN relative to CH_3OH suggests that HOPS 373SW is younger than other hot corinos.

HOPS 373SW, HH 212, and V883 Ori as well as ALMASOP hot corinos are located in the Orion Molecular Cloud Complex, so their initial chemical compositions may be similar. Therefore, the chemical differences between these sources could be considered as the consequence of evolution from envelope to disk.

Compared with the ALMASOP hot corinos, HOPS 373SW has a very high D/H ratio (> 0.1) of CH_3OH , a lower abundance of CH_3CN , and a higher abundance of HCOCH_2OH . On the other hand, HOPS 373SW shows very similar abundances to HH 212, except for CH_3OCHO , whose abundance is higher only by a factor of ~ 2 in HOPS 373SW than HH 212. This may suggest that COMs did not have enough time to be altered in HH 212, and the physical conditions in the disk surface of a Class 0 protostar are not very different from the inner envelope exposed to the radiation from the central Class 0 protostar. However, in V883 Ori, the D/H ratio of CH_3OH is reduced by a factor of 6.5, while the CH_3CHO abundance is enhanced by a factor of 3, compared to HOPS 373SW, although CH_3CN has similar abundance in both sources. The D/H ratios of water and COMs delivered to the protoplanetary disk could be reduced by turbulent mixing as suggested by Furuya et al. (2013).

6. CONCLUSION

We carried out an ALMA observation of HOPS 373SW, which is a brightened and very embedded Class 0 protostar, in band 7, with the same spectral setup used for V883 Ori, which is an eruptive Class I/II disk source. This brightening event provides a unique opportunity to detect the COMs emission lines by expanding the sublimation radius due to the increased luminosity. In addition, comparing COMs emission between two distinct evolutionary stages in the same formation environ-

ment is critical to understanding chemical evolution in the grain surfaces. In HOPS 373SW, eleven COMs as well as HDO and HCCCN have been detected. A rotation velocity structure is well resolved in most of the detected lines although a detailed examination of the kinematics needs to confirm the origin of the rotation. Nevertheless, the size of COMs emission is consistent with the *hot corino* snow line location expected from its luminosity.

According to the comparisons with V883 Ori and other hot corinos, HOPS 373SW shows a highly enhanced D/H ratio of methanol, indicative of a very young hot corino stage. Even doubly and triply deuterated methanols are detected. The ratio between CH_3CN and CH_3OH , which is an evolutionary indicator, is also low in HOPS 373SW, compared to other hot corinos. These chemical characteristics are well consistent with the nature of HOPS 373SW classified as a PACS Bright Red Sources (PBRs) (Stutz et al. 2013), which is considered extremely young. Therefore, HOPS 373SW could be a good place to study the chemistry of COMs in the cold prestellar phase, using the freshly sublimated COMs from grain surfaces.

7. ACKNOWLEDGEMENTS

The authors thank the referee for a helpful and careful report. This work was supported by the National Research Foundation of Korea (NRF) grant funded by the Korea government (MSIT) (grant number 2021R1A2C1011718). G.J.H. is supported by general grants 12173003 and 11773002 awarded by the National Science Foundation of China. D.J. is supported by NRC Canada and by an NSERC Discovery Grant. J.J.T. acknowledges support from NSF AST-1814762. G.B. is supported by SNU Junior Research Fellowship through Seoul National University. The National Radio Astronomy Observatory is a facility of the National Science Foundation operated under cooperative agreement by Associated Universities, Inc.

This paper makes use of the following ALMA data: ADS/JAO.ALMA#2019.1.00386.T. ALMA is a partnership of ESO (representing its member states), NSF (USA) and NINS (Japan), together with NRC (Canada), NSC and ASIAA (Taiwan), and KASI (Republic of Korea), in cooperation with the Republic of Chile. The Joint ALMA Observatory is operated by ESO, AUI/NRAO and NAOJ.

Table 1. Properties of Continuum Sources in HOPS 373SW

	R.A.	Dec.	b_{maj}	b_{min}	Flux density	Peak Intensity	Mass ^a
			mas	mas	mJy	mJy beam ⁻¹	$\times 10^{-3} M_{\odot}$
SW	05:46:30.90483 (0".00046)	-00:02:35.19817 (0".00048)	71.1 (2.6)	61.9 (2.6)	90.4 (1.4)	50.37 (0.55)	20.8 (0.3)
NE	05:46:31.09929 (0".00179)	-00:02:33.0282 (0".00175)	145.8 (7.4)	136.7 (7.8)	75.1 (2.3)	16.57 (0.43)	17.3 (0.5)

The peak positions, deconvolved source sizes, continuum flux density, and peak intensity are measured with the task, imfit in CASA.

The value in parenthesis is the 1 σ error.

^aThe mass of each continuum source is calculated by the equation (1).

Table 2. Identified Lines

Line No.	Formula	Name	Frequency [GHz]	Transition	Einstein-A [$\log_{10}A$]	E_u [K]
spw1						
1	CD ₃ OH	Methanol	335.34538560 (1.10e-03)	11(0,11)-10(1,9)E	-3.68529	133.34479
2	CH ₃ CHO	Acetaldehyde	335.3587225 (2.83e-05)	18(0,18)-17(0,17)A, $v_t=0$	-2.87128	154.85102
3	CH ₃ CHO $v_t=1$	Acetaldehyde	335.38246150 (3.91e-02)	18(0,18)-17(0,17)E $v_t=1$	-2.86455	361.480
4	HDO	Water	335.3955 (2.6e-05)	3(3,1)-4(2,2)	-4.58367	335.26718
5	C ₂ H ₅ OH	Ethanol	335.4406247 (1.84e-05)	33(20,13)-34(17,18),anti	-4.93008	877.18901
	C ₂ H ₅ OH	Ethanol	335.4406247 (1.84e-05)	33(20,14)-34(17,17),anti	-4.93008	877.18901
6	HCOCH ₂ OH	Glycolaldehyde	335.4410822 (7.5e-06)	34(14,20)-34(13,21)	-3.23609	450.0
	HCOCH ₂ OH	Glycolaldehyde	335.441595 (7.5e-06)	34(14,21)-34(13,22)	-3.23609	450.00002
spw2						
7	CHD ₂ OH	Methanol	336.5034229 (2.6e-02)	17(4) ⁻ -17(3) ⁺	-4.11594	356.38737
8	C ₂ H ₅ OH	Ethanol	336.5724107 (2e-06)	19(3,16)-18(3,15),g-	-3.50357	232.33744
9	CH ₃ OH $v_t=2$	Methanol	336.60588900 (1.3e-02)	7(1) ⁺ -6(1) ⁺ $v_t=2$	-3.78622	747.40430
10	C ₂ H ₅ OH	Ethanol	336.6264009 (3.6e-06)	19(2,18)-18(1,17),anti	-3.56713	162.61385
11	CHD ₂ OH	Methanol	336.6270485 (3.0e-02)	18(4) ⁻ -18(3) ⁺	-4.10425	392.42430
12	SO ₂	Sulfur Dioxide	336.6695774 (3.9e-06)	16(7,9)-17(6,12)	-4.23374	245.11422
spw3						
13	CD ₃ OH	Methanol	337.0183286 (1.3e-03)	21(3,18)-21(2,19)	-3.69186	461.01808
14	CH ₃ OH $v_t=2$	Methanol	337.02191700 (4.1e-02)	7(-3)-6(-3)EE $v_t=2$	-3.86646	979.70052
15	CH ₃ OH $v_t=2$	Methanol	337.02957300 (1.8e-02)	7(2) ⁺ -6(2) ⁺ $v_t=2$	-4.23374	941.37640
	CH ₃ OH $v_t=2$	Methanol	337.02966200 (1.8e-02)	7(2) ⁻ -6(2) ⁻ $v_t=2$	-4.23374	941.37641
16	CH ₂ DOH	Methanol	337.0623909 (8.6e-06)	8(2,7)-7(1,6),e0	-5.02093	93.30945
17	C ¹⁷ O	Carbon Monoxide	337.0611298 (1e-05)	J=3-2	-5.6344	32.35323
18	CH ₃ OH $v_t=2$	Methanol	337.06628100 (2.0e-02)	7(4)-6(4)E $v_t=2$	-3.95078	950.98626
19	CH ₃ OH $v_t=2$	Methanol	337.07870700 (1.1e-02)	7(5)-6(5)E $v_t=2$	-4.07598	909.35465
20	CHD ₂ OH	Methanol	337.0983031 (2.1e-02)	4(4) ⁺ -3(3) ⁺	-3.99140	75.09492
	CHD ₂ OH	Methanol	337.0983227 (2.1e-02)	4(4) ⁻ -3(3) ⁻	-3.99140	75.09492
21	CH ₃ OH $v_t=2$	Methanol	337.09891800 (1.8e-02)	7(5) ⁺ -6(5) ⁺ $v_t=2$	-4.08911	935.15562
22	CH ₃ OH $v_t=2$	Methanol	337.11386800 (1.1e-02)	7(1)-6(1)E $v_t=2$	-3.78173	863.67831
spw4						
23	CH ₃ OCHO	Methyl Formate	338.338184 (0.0002)	27(8,19)-26(8,18)E	-3.26914	267.18358
24	CH ₃ OH	Methanol	338.344588 (5e-06)	7(1,7)-6(1,6)E, $v_t=0$	-3.77809	70.55025
25	CH ₃ OCHO	Methyl Formate	338.355792 (0.0001)	27(8,19)-26(8,18)A	-3.26882	267.18572
26	CH ₃ OCHO	Methyl Formate	338.396318 (0.0001)	27(7,21)-26(7,20)E	-3.25943	257.74503
27	CH ₃ OH	Methanol	338.40461 (5e-06)	7(-6,2)-6(-6,1)E, $v_t=0$	-4.34503	243.78966
28	CH ₂ DOH	Methanol	338.4071251 (1.25e-05)	4(4,0)-3(3,0),e0	-4.11124	84.40172
	CH ₂ DOH	Methanol	338.4071284 (1.25e-05)	4(4,1)-3(3,1),e0	-4.11124	84.40172
29	CH ₃ OH	Methanol	338.408698 (5e-06)	7(0,7)-6(0,6)A, $v_t=0$	-3.76908	64.98055
30	C ₂ H ₅ OH	Ethanol	338.4116101 (3.8e-06)	17(7,10)-17(6,11),anti	-3.65839	190.04683
31	CH ₃ OCHO	Methyl Formate	338.414116 (0.0001)	27(7,21)-26(7,20)A	-3.25931	257.74703
32	C ₂ H ₅ OH	Ethanol	338.4168741 (3.8e-06)	17(7,11)-17(6,12),anti	-3.65838	190.0468
33	CH ₃ OH	Methanol	338.430975 (5e-06)	7(6,1)-6(6,0)E, $v_t=0$	-4.34269	253.94589
34	CH ₃ OH	Methanol	338.442367 (5e-06)	7(6,2)-6(6,1)A, $v_t=0$	-4.3436	258.69481
35	CH ₃ OH	Methanol	338.456536 (5e-06)	7(5,3)-6(5,2)E, $v_t=0$	-4.07838	188.99765
36	CH ₂ DOH	Methanol	338.4625377 (9e-06)	9(1,8)-8(2,6),o1	-4.23143	120.01391
37	CH ₃ OH	Methanol	338.475226 (5e-06)	7(-5,2)-6(-5,1)E, $v_t=0$	-4.0781	201.05874
38	CH ₃ OH	Methanol	338.486322 (5e-06)	7(5,2)-6(5,1)A, $v_t=0$	-4.07634	202.88349
39	CH ₃ OH	Methanol	338.504065 (5e-06)	7(4,4)-6(4,3)E, $v_t=0$	-3.94039	152.89245
40	CH ₃ OH	Methanol	338.512632 (5e-06)	7(4,4)-6(4,3)A, $v_t=0$	-3.93973	145.3317
	CH ₃ OH	Methanol	338.512644 (5e-06)	7(4,3)-6(4,2)A, $v_t=0$	-3.93973	145.3317
	CH ₃ OH	Methanol	338.512853 (5e-06)	7(2,6)-6(2,5)A, $v_t=0$	-3.80284	102.70215

Table 2 continued

Table 2 (continued)

Line No.	Formula	Name	Frequency [GHz]	Transition	Einstein-A [$\log_{10}A$]	E_u [K]
41	CH ₃ OH	Methanol	338.530257 (5e-06)	7(-4,3)-6(-4,2)E, $v_t=0$	-3.93784	160.98995
42	CH ₃ OH	Methanol	338.540826 (5e-06)	7(3,5)-6(3,4)A, $v_t=0$	-3.8573	114.79245
43	CH ₃ OH	Methanol	338.543152 (5e-06)	7(3,4)-6(3,3)A, $v_t=0$	-3.8573	114.79257
44	CH ₃ OH	Methanol	338.559963 (5e-06)	7(3,4)-6(3,3)E, $v_t=0$	-3.85418	127.70603
45	CH ₃ OH	Methanol	338.583216 (5e-06)	7(-3,5)-6(-3,4)E, $v_t=0$	-3.85587	112.70842
46	SO ₂	Sulfur Dioxide	338.6118078 (3.5e-06)	20(1,19)-19(2,18)	-3.54241	198.8775
47	CH ₃ OH	Methanol	338.614936 (5e-06)	7(-1,6)-6(-1,5)E, $v_t=0$	-3.76662	86.05157
48	HCOCH ₂ OH	Glycolaldehyde	338.6285049 (6.4e-06)	29(14,15)-29(13,16)	-3.26414	360.71888
	HCOCH ₂ OH	Glycolaldehyde	338.6285126 (6.4e-06)	29(14,16)-29(13,17)	-3.26414	360.71888
49	CH ₃ OH	Methanol	338.639802 (5e-06)	7(2,5)-6(2,4)A, $v_t=0$	-3.80236	102.71572
50	CHD ₂ OH	Methanol	338.6594300 (1.52e-02)	5(2) ⁻ -5(1) ⁺	-3.79102	49.84884
51	C ₂ H ₅ OH	Ethanol	338.6717299 (3.9e-06)	16(7,9)-16(6,10),anti	-3.66791	175.74598
52	C ₂ H ₅ OH	Ethanol	338.6742587 (3.9e-06)	16(7,10)-16(6,11),anti	-3.66791	175.74596
53	CH ₃ OH	Methanol	338.721693 (5e-06)	7(-2,6)-6(-2,5)E, $v_t=0$	-3.80944	87.25749
	CH ₃ OH	Methanol	338.722898 (5e-06)	7(2,5)-6(2,4)E, $v_t=0$	-3.80434	90.91288
54	CH ₂ DOH	Methanol	338.7402165 (1.67e-05)	23(1,22)-23(0,23),e0	-3.92503	600.09684
55	¹³ CH ₃ OH	Methanol	338.759948 (5e-05)	13(0,13)-12(1,12)++	-3.66185	205.94761
spw5						
56	CH ₃ CHO	Acetaldehyde	346.9575559 (2.84e-05)	18(7,12)-17(7,11)A, $v_t=0$	-2.89625	268.60294
	CH ₃ CHO	Acetaldehyde	346.9575577 (2.84e-05)	18(7,11)-17(7,10)A, $v_t=0$	-2.89625	268.60294
57	C ₂ H ₅ OH	Ethanol	346.9626034 (3.2e-06)	21(0,21)-20(1,20),anti	-3.35133	185.84605
58	C ₂ H ₅ OH	Ethanol	346.9745486 (6.7e-06)	17(3,15)-16(2,15),g+	-4.00072	195.1701
59	CH ₃ CHO	Acetaldehyde	346.9955324 (2.82e-05)	18(7,12)-17(7,11)E, $v_t=0$	-2.89625	268.5688
60	CH ₃ CHO	Acetaldehyde	347.0715471 (2.58e-05)	18(6,13)-17(6,12)A, $v_t=0$	-2.87569	239.3968
	CH ₃ CHO	Acetaldehyde	347.0716844 (2.58e-05)	18(6,12)-17(6,11)A, $v_t=0$	-2.87569	239.39681
61	CH ₃ CHO	Acetaldehyde	347.0904015 (2.57e-05)	18(6,12)-17(6,11)E, $v_t=0$	-2.87577	239.39469
62	CH ₃ CHO	Acetaldehyde	347.1326859 (2.58e-05)	18(6,13)-17(6,12)E, $v_t=0$	-2.87563	239.3183
63	C ₂ H ₅ OH	Ethanol	347.1472094 (1.9e-06)	20(6,15)-19(6,14),g+	-3.45039	275.45993
64	C ₂ H ₅ OH	Ethanol	347.1579974 (1.9e-06)	20(6,14)-19(6,13),g+	-3.45038	275.46117
65	CH ₃ CHO	Acetaldehyde	347.1695196 (3.96e-05)	19(0,19)-18(1,18)A, $v_t=0$	-3.66327	171.81276
66	CH ₃ CHO $v_t=1$	Acetaldehyde	347.18241320 (2.99e-02)	18(4,14)-17(4,13)E $v_t=1$	-2.84527	400.374
67	CH ₂ DOH	Methanol	347.1880746 (9.2e-06)	8(5,3)-9(4,6),e1	-5.06349	185.14136
	CH ₂ DOH	Methanol	347.1881494 (9.2e-06)	8(5,4)-9(4,5),e1	-5.06349	185.14137
68	¹³ CH ₃ OH	Methanol	347.188283 (6.4e-05)	14(1,13)-14(0,14)-+	-3.36087	254.25506
69	CH ₃ CHO $v_t=1$	Acetaldehyde	347.21679780 (2.88e-02)	18(5,13)-17(5,12)E $v_t=1$	-2.85918	420.436
70	CH ₂ DOH	Methanol	347.2229918 (9.7e-06)	20(4,16)-20(3,18),e1	-3.87846	521.63257
71	CH ₃ CHO	Acetaldehyde	347.2403963 (3.95e-05)	19(0,19)-18(1,18)E, $v_t=0$	-3.66518	171.88508
72	CH ₃ CHO $v_t=1$	Acetaldehyde	347.25182200 (3.08e-02)	18(5,14)-17(5,13)E $v_t=1$	-2.85886	419.668
73	CH ₃ CHO	Acetaldehyde	347.288264 (2.48e-05)	18(5,14)-17(5,13)A, $v_t=0$	-2.85868	214.69491
74	CH ₃ CHO	Acetaldehyde	347.2948735 (2.48e-05)	18(5,13)-17(5,12)A, $v_t=0$	-2.85857	214.69566
75	SiO	Silicon Monoxide	347.330631 (3.475e-04)	J=8-7	-2.65578	75.01697
76	CH ₃ CHO	Acetaldehyde	347.3457104 (2.48e-05)	18(5,13)-17(5,12)E, $v_t=0$	-2.8586	214.63811
77	CH ₃ CHO	Acetaldehyde	347.3492783 (2.48e-05)	18(5,14)-17(5,13)E, $v_t=0$	-2.85853	214.60878
78	C ₂ H ₅ OH	Ethanol	347.3510886 (6.2e-06)	14(3,12)-13(2,11),anti	-3.80615	99.66183
79	CH ₂ DOH	Methanol	347.3703636 (1.32e-05)	22(2,20)-22(2,21),e1	-7.29364	571.62552
	CH ₂ DOH	Methanol	347.3711668 (9.4e-06)	19(4,16)-19(3,16),e1	-3.88761	478.84197
spw6						
80	CH ₂ DOH	Methanol	349.1838267 (8.2e-06)	13(4,9)-13(3,11),e1	-3.91044	266.96107
81	CH ₃ CN	Methyl Cyanide	349.2123106 (2e-07)	19(6)-18(6)	-2.63745	424.70492
82	CH ₂ DOH	Methanol	349.2422265 (1.38e-05)	21(2,20)-21(1,21),o1	-3.85689	529.71963
83	C ₂ H ₅ OH	Ethanol	349.2844104 (5.5e-06)	9(2,8)-8(1,8),g-	-4.06388	103.72509
84	CH ₃ CN	Methyl Cyanide	349.2860057 (2e-07)	19(5)-18(5)	-2.62274	346.22396
85	CH ₃ CHO $v_t=1$	Acetaldehyde	349.32035150 (3.33e-02)	18(1,17)-17(1,16)E $v_t=1$	-2.81559	369.252
86	CD ₃ OH	Methanol	349.3315497 (7.0e-04)	11(0,11)-10(1,9)E	-3.72285	94.23705

Table 2 continued

Table 2 (*continued*)

Line No.	Formula	Name	Frequency [GHz]	Transition	Einstein-A [$\log_{10}A$]	E_u [K]
87	CH ₂ DOH	Methanol	349.333979 (8.2e-06)	12(4,9)-12(3,9),e1	-3.91862	239.13136
88	CH ₃ CN	Methyl Cyanide	349.3463428 (2e-07)	19(4)-18(4)	-2.61106	281.98778
89	CH ₂ DOH	Methanol	349.3561319 (8.1e-06)	12(4,8)-12(3,10),e1	-3.9182	239.13127
90	CH ₃ CN	Methyl Cyanide	349.3932971 (2e-07)	19(3)-18(3)	-2.60218	232.01121
spw7						
91	CH ₂ DOH	Methanol	350.0902424 (9.4e-06)	5(4,2)-5(3,2),e1	-4.12044	104.24014
	CH ₂ DOH	Methanol	350.0903841 (9.4e-06)	5(4,1)-5(3,3),e1	-4.12044	104.24015
92	¹³ CH ₃ OH	Methanol	350.103118 (5e-05)	1(1,1)-0(0,0)++	-3.48252	16.80241
93	CH ₃ CHO	Acetaldehyde	350.1334296 (2.75e-05)	18(3,15)-17(3,14)A,v _t =0	-2.82551	179.20697
	CH ₃ CHO	Acetaldehyde	350.1343816 (2.75e-05)	18(3,15)-17(3,14)E,v _t =0	-2.82596	179.17508
94	CH ₂ DOH	Methanol	350.1413021 (1.1e-05)	4(4,1)-4(3,1),e1	-4.29793	93.53285
	CH ₂ DOH	Methanol	350.1413378 (1.1e-05)	4(4,0)-4(3,2),e1	-4.29793	93.53285
spw8						
95	CH ₃ CHO	Acetaldehyde	350.3628435 (2.73e-05)	18(1,17)-17(1,16)E,v _t =0	-2.81493	163.45886
96	C ₂ H ₅ OH	Ethanol	350.3650648 (2e-06)	20(4,16)-19(4,15),g+	-3.41113	251.74648
97	¹³ CH ₃ OH	Methanol	350.421585 (5e-05)	8(1,7)-7(2,5)	-4.15313	102.61684
98	CH ₃ OCHO	Methyl Formate	350.44225 (0.0001)	28(8,21)-27(8,20)E	-3.21991	283.90675
99	CH ₃ CHO	Acetaldehyde	350.4457777 (2.74e-05)	18(1,17)-17(1,16)A,v _t =0	-2.81489	163.41752
100	CH ₂ DOH	Methanol	350.4538682 (7.7e-06)	6(2,5)-5(1,5),e1	-3.85626	71.55787
101	CH ₃ OCHO	Methyl Formate	350.45758 (5e-05)	28(8,21)-27(8,20)A	-3.21978	283.9095
102	CHD ₂ OH	Methanol	350.4673839 (2.8e-02)	16(1) ⁺ -15(2) ⁺	-4.20845	276.34756

Note. Species with the same numbering are observed as a blended line.

Table 3. Tentatively Identified Lines

Line No.	Formula	Name	Frequency [GHz]	Transition	Einstein-A [$\log_{10}A$]	E_u [K]
spw1						
1	CH ₂ DCHO	Acetaldehyde	335.40589500 (1.0e-02)	19(0,19)-18(0,18)	-2.87877	163.435
spw2						
2	HCCCN	Cyanoacetylene	336.52008400 (1.0e-02)	J=37-36	-2.51613	306.906
spw3						
3	CH ₃ CHO $v_t=2$	Acetaldehyde	337.08157220 (1.43e-01)	18(1,18)-17(1,17)	-2.88207	526.134
spw4						
4	CH ₃ CHO $v_t=2$	Acetaldehyde	338.31785810 (1.61e-01)	18(5,14)-17(5,13)	-2.86934	605.150
5	³⁴ SO ₂	Sulfur Dioxide	338.32035640 (4.2e-03)	13(2,12)-12(1,11)	-3.64397	92.449
spw5						
6	CH ₃ OD	Methanol	347.308432 (1.39e-04)	5(4) ⁻ -6(3) ⁻	- ^a	104.311
spw8						
7	CD ₃ OH $v_t=1$	Methanol	350.430949 (1.0e-03)	9(1,8)A-8(1,7)A	-3.71041	384.41981

^a The information the CH₃OD line is from Anderson et al. (1988) and Duan et al. (2003), which do not provide its Einstein-A coefficient.

Table 4. Results of XCLASS fittings

Species	Formula	Column density ^a [cm ⁻²]	T_{rot} [K]	X(<i>w.r.t.</i> H ₂)	X(<i>w.r.t.</i> CH ₃ OH) ^b
Identified					
Methanol	CH ₃ OH	$8.04^{+1.06}_{-0.69} \times 10^{17}$	$75.9^{+0.53}_{-4.24}$	9.03×10^{-8}	-
	CH ₃ OH $v_t=2$	$1.11^{+2.97}_{-0.16} \times 10^{18}$	$200^{+6.04}_{-11.3}$	1.25×10^{-7}	3.61×10^{-1}
	CD ₃ OH	$6.20^{+1.65}_{-1.84} \times 10^{16}$	$126^{+2.53}_{-2.07}$	6.97×10^{-9}	2.02×10^{-2}
	¹³ CH ₃ OH	$5.11^{+0.70}_{-1.33} \times 10^{16}$	$98.0^{+2.79}_{-4.19}$	5.75×10^{-9}	1.67×10^{-2}
	CH ₂ DOH	$4.03^{+0.72}_{-0.59} \times 10^{17}$	$199^{+4.79}_{-5.85}$	4.53×10^{-8}	1.31×10^{-1}
	CHD ₂ OH	$3.03^{+0.98}_{-0.42} \times 10^{17}$	$237^{+4.78}_{-4.78}$	3.40×10^{-8}	9.87×10^{-2}
Acetaldehyde	CH ₃ CHO	$1.97^{+0.37}_{-0.54} \times 10^{16}$	$129^{+4.47}_{-10.4}$	2.21×10^{-9}	6.41×10^{-3}
	CH ₃ CHO $v_t=1$	$2.06^{+0.60}_{-0.56} \times 10^{16}$	$210^{+47.1}_{-47.1}$	2.31×10^{-9}	6.72×10^{-3}
Methyl Formate	CH ₃ OCHO	$1.53^{+0.41}_{-0.22} \times 10^{17}$	$445^{+3.46}_{-6.43}$	1.71×10^{-8}	4.98×10^{-2}
Ethanol	C ₂ H ₅ OH	$5.07^{+1.54}_{-0.68} \times 10^{16}$	$116^{+6.84}_{-4.56}$	5.70×10^{-9}	1.65×10^{-2}
Methyl Cyanide	CH ₃ CN	$2.24^{+0.52}_{-0.42} \times 10^{15}$	$207^{+10.8}_{-7.35}$	2.51×10^{-10}	7.29×10^{-4}
Glycolaldehyde	HCOCH ₂ OH	$2.09^{+0.35}_{-0.53} \times 10^{16}$	$116^{+6.78}_{-2.90}$	2.35×10^{-9}	6.81×10^{-3}
Water	HDO ^c	$1.40^{+0.17}_{-0.12} \times 10^{17}$	100	1.58×10^{-8}	4.56×10^{-2}
Sulfur Dioxide	SO ₂	$2.92^{+0.45}_{-0.68} \times 10^{17}$	$62.0^{+3.65}_{-1.04}$	3.29×10^{-8}	9.51×10^{-2}
Silicon Monoxide	SiO ^c	$4.96^{+0.60}_{-0.24} \times 10^{13}$	100	5.58×10^{-12}	1.62×10^{-5}
Tentatively Identified					
Acetaldehyde	CH ₂ DCHO ^c	$6.24^{+0.48}_{-0.24} \times 10^{15}$	100	7.01×10^{-10}	2.03×10^{-3}
Cyanoacetylene	HCCCN ^c	$1.06^{+0.06}_{-0.22} \times 10^{15}$	100	1.19×10^{-10}	3.45×10^{-4}
Sulfur Dioxide	³⁴ SO ₂ ^c	$4.69^{+0.29}_{-0.66} \times 10^{15}$	100	5.27×10^{-10}	1.53×10^{-3}
Methanol	CD ₃ OH $v_t=1$ ^c	$3.73^{+0.58}_{-0.34} \times 10^{17}$	100	4.19×10^{-8}	1.21×10^{-1}

Note. Linewidths were fixed as 2 km s⁻¹.

^a The uncertainty of column density corresponds to the 1 σ error.

^b X(*w.r.t.* CH₃OH) was calculated using the derived column density of ¹³CH₃OH and the ¹²C/¹³C ratio of 60.

^c Only one transition was detected for these molecules, so the temperature was fixed as 100 K in the XCLASS fitting.

Table 5. D/H ratio

	Observed Ratio	D/H [%] ^a
CH ₂ DOH/CH ₃ OH ^b	0.36	12
CHD ₂ OH/CH ₃ OH	0.27	30
CD ₃ OH/CH ₃ OH	0.06	38
CH ₂ DCHO/CH ₃ CHO	0.32	11

^a Statistical correction has applied to measure the D/H ratio (Parise et al. 2004; Appendix B of Manigand et al. 2019)

^b The CH₃OH column density was calculated using the CH₃OH $v_7=2$ lines.

Table 6. X(*w.r.t* CH₃OH) in Various Sources

Molecules	Sources							
	HOPS 373SW ^a	ALMASOP ^{a,b}	HH 212 ^{a,c}	V883 Ori ^{a,d}	IRAS16293B ^e	PEACHES ^f	BHR71 ^g	L483 ^{a,h}
CH ₂ DOH	$1.3^{+0.3}_{-0.4} \times 10^{-1}$	2.9×10^{-2}	$1.0^{+0.2}_{-0.2} \times 10^{-1}$	$2.0^{+0.1}_{-0.1} \times 10^{-2}$	$7.1^{+2.1}_{-2.1} \times 10^{-2}$	–	2.9×10^{-2}	$2.7^{+0.8}_{-0.8} \times 10^{-2}$
CH ₃ CHO	$6.4^{+1.5}_{-2.4} \times 10^{-3}$	1.7×10^{-3}	$9.6^{+1.3}_{-1.3} \times 10^{-3}$	$2.0^{+0.1}_{-0.1} \times 10^{-2}$	$1.2^{+0.4}_{-0.4} \times 10^{-2}$	$8.9^{+27.6}_{-6.7} \times 10^{-2}$	–	$5.3^{+1.5}_{-1.5} \times 10^{-3}$
CH ₃ OCHO	$5.0^{+1.5}_{-1.5} \times 10^{-2}$	1.6×10^{-2}	$2.1^{+0.5}_{-0.5} \times 10^{-2}$	$7.5^{+0.1}_{-0.1} \times 10^{-2}$	$2.6^{+0.8}_{-0.8} \times 10^{-2}$	$2.2^{+4.4}_{-1.5} \times 10^{-1}$	1.8×10^{-2}	$8.7^{+2.5}_{-2.5} \times 10^{-3}$
C ₂ H ₅ OH	$1.7^{+0.6}_{-0.5} \times 10^{-2}$	2.4×10^{-2}	$1.7^{+0.3}_{-0.3} \times 10^{-2}$	–	$2.3^{+0.7}_{-0.7} \times 10^{-2}$	$1.7^{+3.5}_{-1.2} \times 10^{-1}$	5.4×10^{-3}	$6.7^{+1.9}_{-1.9} \times 10^{-3}$
CH ₃ CN	$7.3^{+2.0}_{-2.3} \times 10^{-4}$	–	–	$7.8^{+0.1}_{-0.1} \times 10^{-4}$	$4.0^{+1.0}_{-1.2} \times 10^{-3}$	$1.2^{+2.6}_{-0.8} \times 10^{-2}$	–	–
HCOCH ₂ OH	$6.8^{+1.5}_{-2.5} \times 10^{-3}$	–	–	–	$3.4^{+1.0}_{-1.0} \times 10^{-3}$	$1.4^{+2.8}_{-0.9} \times 10^{-2}$	–	–
HDO	$4.6^{+0.8}_{-1.2} \times 10^{-2}$	–	–	1.2×10^{-2}	–	–	–	–

Molecules	HOPS 373SW ^a	5 sources in ALMASOP survey ^a				
		G192	G205S1A HOPS-358-A	G208N1 HOPS-87	G210WA HOPS-168-A	G211S HOPS-288-A-A
CH ₂ DOH	$1.3^{+0.3}_{-0.4} \times 10^{-1}$	$2.5^{+0.1}_{-0.1} \times 10^{-2}$	$2.1^{+0.3}_{-0.1} \times 10^{-2}$	$3.0^{+1.2}_{-2.1} \times 10^{-2}$	$3.2^{+0.3}_{-0.2} \times 10^{-2}$	$4.4^{+0.1}_{-0.4} \times 10^{-2}$
CH ₃ CHO	$6.4^{+1.5}_{-2.4} \times 10^{-3}$	$8.2^{+0.6}_{-0.3} \times 10^{-4}$	$1.2^{+0.1}_{-0.2} \times 10^{-3}$	$1.4^{+0.1}_{-0.1} \times 10^{-3}$	$1.4^{+0.1}_{-0.1} \times 10^{-3}$	$6.1^{+0.2}_{-0.8} \times 10^{-3}$
CH ₃ OCHO	$5.0^{+1.5}_{-1.5} \times 10^{-2}$	$1.3^{+0.1}_{-0.2} \times 10^{-2}$	$1.4^{+0.1}_{-0.4} \times 10^{-2}$	$1.2^{+0.1}_{-0.3} \times 10^{-2}$	$7.8^{+0.1}_{-0.8} \times 10^{-3}$	$2.1^{+0.1}_{-0.2} \times 10^{-2}$
C ₂ H ₅ OH	$1.7^{+0.6}_{-0.5} \times 10^{-2}$	–	–	$2.5^{+0.1}_{-0.1} \times 10^{-2}$	–	$2.4^{+0.1}_{-0.1} \times 10^{-2}$
CH ₃ CN ⁱ	$7.3^{+2.0}_{-2.3} \times 10^{-4}$	–	$5.1^{+0.6}_{-0.2} \times 10^{-3}$	$6.8^{+0.1}_{-0.2} \times 10^{-3}$	–	$9.6^{+0.4}_{-3.1} \times 10^{-3}$
HCOCH ₂ OH	$6.8^{+1.5}_{-2.5} \times 10^{-3}$	–	–	$3.6^{+0.2}_{-0.2} \times 10^{-3}$	–	–

^a X(*w.r.t* CH₃OH) was calculated using the derived column density of ¹³CH₃OH and the ¹²C/¹³C ratio of 60.

^b X(*w.r.t* CH₃OH) are adopted from Figure 7 of Hsu et al. (2022) and scaled down by a factor of 1.2 to adopt the ¹²C/¹³C ratio of 60.

^c Lee et al. (2019a).

^d Lee et al. (2019b). The HDO abundance is derived from a tentative detection.

^e X(*w.r.t* CH₃OH) was calculated using the derived column density of CH₃¹⁸OH and the ¹⁶O/¹⁸O ratio of 560 (Jørgensen et al. 2018, 2020). CH₂DOH abundance is adopted from (Jørgensen et al. 2018).

^f Yang et al. (2021).

^g Yang et al. (2020). The abundances are estimated from the obtained column densities assuming T_{ex}=100 K.

^h Jacobsen et al. (2019).

ⁱ X(*w.r.t* CH₃CN) of ALMASOP sources were calculated using the derived column density of ¹³CH₃CN and the ¹²C/¹³C ratio of 60.

REFERENCES

- Agundez, M., Marcelino, N., Cernicharo, J., Roueff, E., & Tafalla, M. 2019, *A&A*, 625, A147, doi: [10.1051/0004-6361/201935164](https://doi.org/10.1051/0004-6361/201935164)
- Aikawa, Y., Wakelam, V., Hersant, F., Garrod, R. T., & Herbst, E. 2012, *ApJ*, 760, 40, doi: [10.1088/0004-637X/760/1/40](https://doi.org/10.1088/0004-637X/760/1/40)
- Altwegg, K., Balsiger, H., Berthelier, J. J., et al. 2017, *MNRAS*, 469, S130, doi: [10.1093/mnras/stx1415](https://doi.org/10.1093/mnras/stx1415)
- Anderson, T., Crownover, R. L., Herbst, E., & De Lucia, F. C. 1988, *ApJS*, 67, 135, doi: [10.1086/191269](https://doi.org/10.1086/191269)
- Antoniucci, S., Giannini, T., Li Causi, G., & Lorenzetti, D. 2014, *ApJ*, 782, 51, doi: [10.1088/0004-637X/782/1/51](https://doi.org/10.1088/0004-637X/782/1/51)
- Artur de la Villarmois, E., Jørgensen, J. K., Kristensen, L. E., et al. 2019, *A&A*, 626, A71, doi: [10.1051/0004-6361/201834877](https://doi.org/10.1051/0004-6361/201834877)
- Belloche, A., Maury, A. J., Maret, S., et al. 2020, *A&A*, 635, A198, doi: [10.1051/0004-6361/201937352](https://doi.org/10.1051/0004-6361/201937352)
- Bianchi, E., Codella, C., Ceccarelli, C., et al. 2017, *MNRAS*, 467, 3011, doi: [10.1093/mnras/stx252](https://doi.org/10.1093/mnras/stx252)
- Bisschop, S. E., Jørgensen, J. K., van Dishoeck, E. F., & de Wachter, E. B. M. 2007, *A&A*, 465, 913, doi: [10.1051/0004-6361:20065963](https://doi.org/10.1051/0004-6361:20065963)
- Bonfand, M., Belloche, A., Garrod, R. T., et al. 2019, *A&A*, 628, A27, doi: [10.1051/0004-6361/201935523](https://doi.org/10.1051/0004-6361/201935523)
- Ceccarelli, C., Caselli, P., Herbst, E., Tielens, A. G. G. M., & Caux, E. 2007, in *Protostars and Planets V*, ed. B. Reipurth, D. Jewitt, & K. Keil, 47, doi: [10.48550/arXiv.astro-ph/0603018](https://doi.org/10.48550/arXiv.astro-ph/0603018)
- Chacón-Tanarro, A., Caselli, P., Bizzocchi, L., et al. 2019, *A&A*, 622, A141, doi: [10.1051/0004-6361/201832703](https://doi.org/10.1051/0004-6361/201832703)
- Chang, Q., & Herbst, E. 2016, *ApJ*, 819, 145, doi: [10.3847/0004-637X/819/2/145](https://doi.org/10.3847/0004-637X/819/2/145)
- Chiang, E. I., & Goldreich, P. 1997, *ApJ*, 490, 368, doi: [10.1086/304869](https://doi.org/10.1086/304869)
- Coudert, L. H., Motiyenko, R. A., Margulès, L., & Tchana Kwabia, F. 2021, *Journal of Molecular Spectroscopy*, 381, 111515, doi: [10.1016/j.jms.2021.111515](https://doi.org/10.1016/j.jms.2021.111515)
- Drozdovskaya, M. N., Coudert, L. H., Margulès, L., et al. 2022, *A&A*, 659, A69, doi: [10.1051/0004-6361/202142863](https://doi.org/10.1051/0004-6361/202142863)
- Drozdovskaya, M. N., Schroeder I, I. R. H. G., Rubin, M., et al. 2021, *MNRAS*, 500, 4901, doi: [10.1093/mnras/staa3387](https://doi.org/10.1093/mnras/staa3387)
- Duan, Y. B., Ozier, I., Tsunekawa, S., & Takagi, K. 2003, *Journal of Molecular Spectroscopy*, 218, 95, doi: [10.1016/S0022-2852\(02\)00046-2](https://doi.org/10.1016/S0022-2852(02)00046-2)
- Evans, Neal J., I., Di Francesco, J., Lee, J.-E., et al. 2015, *ApJ*, 814, 22, doi: [10.1088/0004-637X/814/1/22](https://doi.org/10.1088/0004-637X/814/1/22)
- Fischer, W. J., Safron, E., & Megeath, S. T. 2019, *ApJ*, 872, 183, doi: [10.3847/1538-4357/ab01dc](https://doi.org/10.3847/1538-4357/ab01dc)
- Francis, L., Johnstone, D., Herczeg, G., Hunter, T. R., & Harsono, D. 2020, *AJ*, 160, 270, doi: [10.3847/1538-3881/abbe1a](https://doi.org/10.3847/1538-3881/abbe1a)
- Furlan, E., Fischer, W. J., Ali, B., et al. 2016, *The Astrophysical Journal Supplement Series*, 224, 5, doi: [10.3847/0067-0049/224/1/5](https://doi.org/10.3847/0067-0049/224/1/5)
- Furuya, K., Aikawa, Y., Nomura, H., Hersant, F., & Wakelam, V. 2013, *ApJ*, 779, 11, doi: [10.1088/0004-637X/779/1/11](https://doi.org/10.1088/0004-637X/779/1/11)
- Garrod, R. T., & Herbst, E. 2006, *A&A*, 457, 927, doi: [10.1051/0004-6361:20065560](https://doi.org/10.1051/0004-6361:20065560)
- Harsono, D., Bjerke, P., van der Wiel, M. H. D., et al. 2018, *Nature Astronomy*, 2, 646, doi: [10.1038/s41550-018-0497-x](https://doi.org/10.1038/s41550-018-0497-x)
- Hartmann, L., & Kenyon, S. J. 1996, *ARA&A*, 34, 207, doi: [10.1146/annurev.astro.34.1.207](https://doi.org/10.1146/annurev.astro.34.1.207)
- Hsu, S.-Y., Liu, S.-Y., Liu, T., et al. 2022, *ApJ*, 927, 218, doi: [10.3847/1538-4357/ac49e0](https://doi.org/10.3847/1538-4357/ac49e0)
- Ilyushin, V. V., Müller, H. S. P., Jørgensen, J. K., et al. 2022, *A&A*, 658, A127, doi: [10.1051/0004-6361/202142326](https://doi.org/10.1051/0004-6361/202142326)
- Imai, M., Sakai, N., Oya, Y., et al. 2016, *ApJL*, 830, L37, doi: [10.3847/2041-8205/830/2/L37](https://doi.org/10.3847/2041-8205/830/2/L37)
- Jacobsen, S. K., Jørgensen, J. K., Di Francesco, J., et al. 2019, *A&A*, 629, A29, doi: [10.1051/0004-6361/201833214](https://doi.org/10.1051/0004-6361/201833214)
- Jin, M., & Garrod, R. T. 2020, *ApJS*, 249, 26, doi: [10.3847/1538-4365/ab9ec8](https://doi.org/10.3847/1538-4365/ab9ec8)
- Johnstone, D., Herczeg, G. J., Mairs, S., et al. 2018, *The Astrophysical Journal*, 854, 31, doi: [10.3847/1538-4357/aaa764](https://doi.org/10.3847/1538-4357/aaa764)
- Jørgensen, J. K., Belloche, A., & Garrod, R. T. 2020, *ARA&A*, 58, 727, doi: [10.1146/annurev-astro-032620-021927](https://doi.org/10.1146/annurev-astro-032620-021927)
- Jørgensen, J. K., van der Wiel, M. H. D., Coutens, A., et al. 2016, *A&A*, 595, A117, doi: [10.1051/0004-6361/201628648](https://doi.org/10.1051/0004-6361/201628648)
- Jørgensen, J. K., Müller, H. S. P., Calcutt, H., et al. 2018, *A&A*, 620, A170, doi: [10.1051/0004-6361/201731667](https://doi.org/10.1051/0004-6361/201731667)
- Kahane, C., Jaber Al-Edhari, A., Ceccarelli, C., et al. 2018, *ApJ*, 852, 130, doi: [10.3847/1538-4357/aa9e88](https://doi.org/10.3847/1538-4357/aa9e88)
- Kang, M., Choi, M., Stutz, A. M., & Tatematsu, K. 2015, *ApJ*, 814, 31, doi: [10.1088/0004-637X/814/1/31](https://doi.org/10.1088/0004-637X/814/1/31)
- Langer, W. D., & Penzias, A. A. 1993, *ApJ*, 408, 539, doi: [10.1086/172611](https://doi.org/10.1086/172611)
- Lee, C.-F., Codella, C., Li, Z.-Y., & Liu, S.-Y. 2019a, *ApJ*, 876, 63, doi: [10.3847/1538-4357/ab15db](https://doi.org/10.3847/1538-4357/ab15db)
- Lee, J.-E., & Bergin, E. A. 2015, *ApJ*, 799, 104, doi: [10.1088/0004-637X/799/1/104](https://doi.org/10.1088/0004-637X/799/1/104)

- Lee, J.-E., Lee, S., Baek, G., et al. 2019b, *Nature Astronomy*, 3, 314, doi: [10.1038/s41550-018-0680-0](https://doi.org/10.1038/s41550-018-0680-0)
- Lee, S., Lee, J.-E., Aikawa, Y., Herczeg, G., & Johnstone, D. 2020, *ApJ*, 889, 20, doi: [10.3847/1538-4357/ab5a7e](https://doi.org/10.3847/1538-4357/ab5a7e)
- Lee, Y.-H., Johnstone, D., Lee, J.-E., et al. 2021, *ApJ*, 920, 119, doi: [10.3847/1538-4357/ac1679](https://doi.org/10.3847/1538-4357/ac1679)
- Leemker, M., van't Hoff, M. L. R., Trapman, L., et al. 2021, *A&A*, 646, A3, doi: [10.1051/0004-6361/202039387](https://doi.org/10.1051/0004-6361/202039387)
- Lin, Y., Spezzano, S., & Caselli, P. 2023, *A&A*, 669, L6, doi: [10.1051/0004-6361/202245524](https://doi.org/10.1051/0004-6361/202245524)
- López-Sepulcre, A., Sakai, N., Neri, R., et al. 2017, *A&A*, 606, A121, doi: [10.1051/0004-6361/201630334](https://doi.org/10.1051/0004-6361/201630334)
- Lucas, P. W., Smith, L. C., Contreras Peña, C., et al. 2017, *MNRAS*, 472, 2990, doi: [10.1093/mnras/stx2058](https://doi.org/10.1093/mnras/stx2058)
- Manigand, S., Calcutt, H., Jørgensen, J. K., et al. 2019, *A&A*, 623, A69, doi: [10.1051/0004-6361/201832844](https://doi.org/10.1051/0004-6361/201832844)
- McMullin, J. P., Waters, B., Schiebel, D., Young, W., & Golap, K. 2007, in *Astronomical Society of the Pacific Conference Series*, Vol. 376, *Astronomical Data Analysis Software and Systems XVI*, ed. R. A. Shaw, F. Hill, & D. J. Bell, 127
- Nomura, H., Furuya, K., Cordiner, M. A., et al. 2022, *arXiv e-prints*, arXiv:2203.10863, doi: [10.48550/arXiv.2203.10863](https://doi.org/10.48550/arXiv.2203.10863)
- Öberg, K. I., Fayolle, E. C., Reiter, J. B., & Cyganowski, C. 2014, *Faraday Discussions*, 168, 81, doi: [10.1039/C3FD00146F](https://doi.org/10.1039/C3FD00146F)
- Ossenkopf, V., & Henning, T. 1994, *A&A*, 291, 943
- Parise, B., Castets, A., Herbst, E., et al. 2004, *A&A*, 416, 159, doi: [10.1051/0004-6361:20034490](https://doi.org/10.1051/0004-6361:20034490)
- Park, W., Lee, J.-E., Contreras Peña, C., et al. 2021, *ApJ*, 920, 132, doi: [10.3847/1538-4357/ac1745](https://doi.org/10.3847/1538-4357/ac1745)
- Rebull, L. M., Cody, A. M., Covey, K. R., et al. 2014, *AJ*, 148, 92, doi: [10.1088/0004-6256/148/5/92](https://doi.org/10.1088/0004-6256/148/5/92)
- Sahu, D., Liu, S.-Y., Su, Y.-N., et al. 2019, *ApJ*, 872, 196, doi: [10.3847/1538-4357/aaffda](https://doi.org/10.3847/1538-4357/aaffda)
- Sakai, N., Oya, Y., Sakai, T., et al. 2014, *ApJL*, 791, L38, doi: [10.1088/2041-8205/791/2/L38](https://doi.org/10.1088/2041-8205/791/2/L38)
- Scholz, A., Froebrich, D., & Wood, K. 2013, *MNRAS*, 430, 2910, doi: [10.1093/mnras/stt091](https://doi.org/10.1093/mnras/stt091)
- Shingledecker, C. N., Tennis, J., Le Gal, R., & Herbst, E. 2018, *ApJ*, 861, 20, doi: [10.3847/1538-4357/aac5ee](https://doi.org/10.3847/1538-4357/aac5ee)
- Stutz, A. M., Tobin, J. J., Stanke, T., et al. 2013, *The Astrophysical Journal*, 767, 36, doi: [10.1088/0004-637X/767/1/36](https://doi.org/10.1088/0004-637X/767/1/36)
- Taquet, V., Charnley, S. B., & Sipilä, O. 2014, *ApJ*, 791, 1, doi: [10.1088/0004-637X/791/1/1](https://doi.org/10.1088/0004-637X/791/1/1)
- Taquet, V., Bianchi, E., Codella, C., et al. 2019, *A&A*, 632, A19, doi: [10.1051/0004-6361/201936044](https://doi.org/10.1051/0004-6361/201936044)
- Tobin, J. J., Stutz, A. M., Megeath, S. T., et al. 2015, *ApJ*, 798, 128, doi: [10.1088/0004-637X/798/2/128](https://doi.org/10.1088/0004-637X/798/2/128)
- Tobin, J. J., Sheehan, P. D., Megeath, S. T., et al. 2020, *ApJ*, 890, 130, doi: [10.3847/1538-4357/ab6f64](https://doi.org/10.3847/1538-4357/ab6f64)
- Tobin, J. J., van't Hoff, M. L. R., Leemker, M., et al. 2023, *Nature*, 615, 227, doi: [10.1038/s41586-022-05676-z](https://doi.org/10.1038/s41586-022-05676-z)
- van Gelder, M. L., Tabone, B., Tychoniec, L., et al. 2020, *A&A*, 639, A87, doi: [10.1051/0004-6361/202037758](https://doi.org/10.1051/0004-6361/202037758)
- van't Hoff, M. L. R., Tobin, J. J., Trapman, L., et al. 2018, *ApJL*, 864, L23, doi: [10.3847/2041-8213/aadb8a](https://doi.org/10.3847/2041-8213/aadb8a)
- van't Hoff, M. L. R., Harsono, D., Tobin, J. J., et al. 2020, *ApJ*, 901, 166, doi: [10.3847/1538-4357/abb1a2](https://doi.org/10.3847/1538-4357/abb1a2)
- van't Hoff, M. L. R., Harsono, D., van Gelder, M. L., et al. 2022, *ApJ*, 924, 5, doi: [10.3847/1538-4357/ac3080](https://doi.org/10.3847/1538-4357/ac3080)
- Williams, J. P., & Cieza, L. A. 2011, *ARA&A*, 49, 67, doi: [10.1146/annurev-astro-081710-102548](https://doi.org/10.1146/annurev-astro-081710-102548)
- Yang, Y.-L., Evans, Neal J., I., Smith, A., et al. 2020, *ApJ*, 891, 61, doi: [10.3847/1538-4357/ab7201](https://doi.org/10.3847/1538-4357/ab7201)
- Yang, Y.-L., Sakai, N., Zhang, Y., et al. 2021, *ApJ*, 910, 20, doi: [10.3847/1538-4357/abdf6](https://doi.org/10.3847/1538-4357/abdf6)
- Yen, H.-W., Liu, H. B., Gu, P.-G., et al. 2016, *ApJL*, 820, L25, doi: [10.3847/2041-8205/820/2/L25](https://doi.org/10.3847/2041-8205/820/2/L25)
- Yoon, S.-Y., Herczeg, G. J., Lee, J.-E., et al. 2022, *ApJ*, 929, 60, doi: [10.3847/1538-4357/ac5632](https://doi.org/10.3847/1538-4357/ac5632)
- Zakri, W., Megeath, S. T., Fischer, W. J., et al. 2022, *ApJL*, 924, L23, doi: [10.3847/2041-8213/ac46ae](https://doi.org/10.3847/2041-8213/ac46ae)